Supporting information

Hydrogen-bonded organic supramolecular layered structure for efficient Grotthuss proton conduction in aqueous proton batteries

Cheng-Yueh Wang,[‡[a]] Shih-Cheng Lo,[‡[a]] Pakin Chinphuad,[[a]] Li-Ying Chen,[[a]] Anton S. Pozdeev,[[b]] Alexander S. Ivanov,*[[c]] Ilja Popovs,[[c]] Pilgun Oh[[d]] and Watchareeya Kaveevivitchai*[[a,e]]

[a] Department of Chemical Engineering
and Hierarchical Green-Energy Materials Research Center
National Cheng Kung University
Tainan City 70101, Taiwan

[b] Department of Chemical and Biomolecular Engineering
Vanderbilt University
Nashville, TN 37235, USA

[c] Department of Nuclear Engineering
University of Tennessee
Knoxville, TN 37996, USA

[d] Department of Smart Green Technology Engineering
and Department of Nanotechnology Engineering
Pukyong National University
Busan 48547, Republic of Korea

[e] Academy of Innovative Semiconductor and Sustainable Manufacturing
National Cheng Kung University
Tainan City 70101, Taiwan

‡ These authors contributed equally to this work.

* To whom correspondence should be addressed. E-mail: aivanov@utk.edu, wkaveechai@mail.ncku.edu.tw

General methods and materials

Starting materials and solvents were purchased and used without further purification from commercial suppliers (Sigma-Aldrich and Alfa Aesar). The compound HATAQ was prepared by a reaction between 2,3-diamino-1,4-naphthoquinone and cyclohexane hexaketone according to our original procedure reported previously.[1] Powder X-ray diffraction (PXRD) patterns were collected on Bruker D8 Advance ECO with Cu Kα radiation using a silicon substrate zero-background sample holder. Samples were dried at 120 ºC in a vacuum oven overnight before measurements. Fourier-transform infrared (FT-IR) spectra were recorded on PerkinElmer Frontier MIR spectrometer. The electrodes were washed with DI water and dried before measurements. X-ray photoelectron spectroscopy (XPS) measurements were performed on ULVAC PHI 5000 VersaProbe III with Al Kα (1487 eV) as an X-ray source. Survey scans were collected with a pass energy of 100 eV, followed by high-resolution scans of the C 1s, N 1s and O 1s regions with a pass energy of 20 eV. All spectra were charge-corrected relative to the C 1s component at 284.6 eV binding energy and analyzed using CasaXPS software. Scanning electron microscopy (SEM) images were collected on a SU8010 HR-FESEM scanning electron microscope. Prior to the testing, the samples underwent platinum-sputtering to enhance the conductivity. Scanning transmission electron microscopy (STEM) and energy dispersive X-ray spectroscopy (EDS) were carried out on JEOL JEM-2010 electron microscope. The ^{1}H solid-state nuclear magnetic resonance (NMR) spectra were recorded on a Bruker Avance III HD 400MHz NMR spectrometer.

Synthesis of HATAQ

HATAQ was synthesized according to our reported procedure as shown in Scheme S1.[1] 2,3-diamino-1,4-naphthoquinone (61.2 g, 325 mmol) was first dissolved in degassed glacial acetic acid (1500 mL), and hexaketone octahydrate (31.2 g, 100 mmol) was added to the solution. The reaction mixture was heated at reflux at 120 ºC for 24 h under argon atmosphere. The mixture was then cooled to 60 ºC followed by filtration to collect the dark brown solid residue. The solid was washed successively with fresh glacial acetic acid (200 mL), ethanol (200 mL) and acetone (200 mL), followed by vacuum drying for 24 h. The resulting black solid was suspended in water and dried under vacuum. The black solid was suspended in 250 mL of 25% HNO_3 and then heated at reflux at 100 °C for 2 h while stirring vigorously. During this process, color change can be observed from dark brown to dark orange. After cooling to room temperature, the solid product was obtained by filtration using a glass filter. The filter cake was washed with deionized water (5 x 500 mL) and then dried overnight under dynamic vacuum. 87% yield of the final product (54.3 g) was obtained as yellow-orange powder.

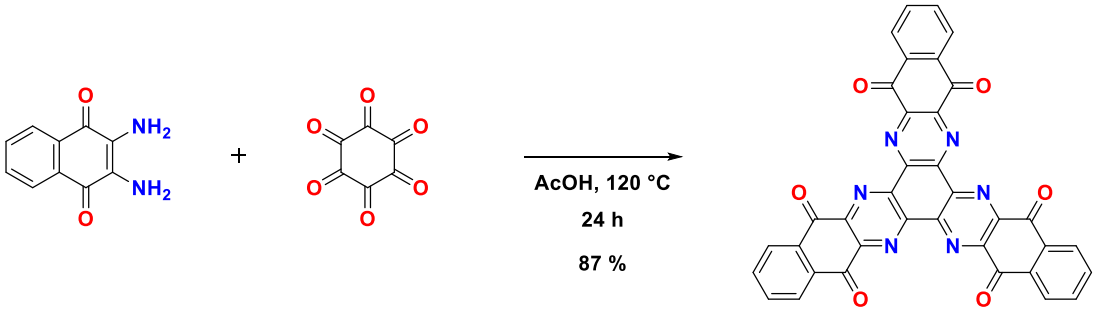

Scheme S1 The synthesis route to prepare HATAQ.

Electrochemical measurements

The active material HATAQ was combined with Ketjen black and poly(vinylidenedifluoride) PVDF in a mass ratio of 7:2:1, respectively. The mixture was ground by using an agate mortar and pestle. *N*-methyl-2-pyrrolidinone (NMP) were added to form a slurry, which was then uniformly coated onto half of the carbon paper (MGL280) current collector (area of 1 cm × 1 cm on a rectangular carbon paper with 1 cm × 2 cm dimension). The mass loading of active material was ~2 mg. The coated electrodes were then dried under vacuum at 100 °C overnight. Three-electrode cells were assembled with platinum foil counter electrode and Hg/Hg_2SO_4 reference electrode. 4 M H_2SO_4 aqueous solution was used as the electrolyte (~6 mL in 20 mL glass cell). The cells were rested for 3 h before testing. All the electrochemical tests including galvanostatic measurements, cyclic voltammetry (CV), galvanostatic intermittent titration technique (GITT) and electrochemical impedance spectroscopy (EIS), were done on a VMP3 potentiostat (BioLogic). EIS measurements were carried out over a frequency range of 70 kHz−10 mHz. For activation energy calculations, the cells were placed in a temperature chamber and EIS data were collected at 25, 30, 40 and 50 °C. The cells were allowed to equilibrate for at least 1 h at each temperature. For CV kinetic studies, a pre-polished glassy carbon working electrode (3 mm diameter) was used. 3 μL of homogeneous suspension (5.87 mg active material, 1.68 mg Ketjen black and 0.84 mg PVDF in 1 mL NMP) was dropped on the electrode and dried at 50 °C in vacuum overnight.

Multiple-step chronoamperometry

Multiple-step chronoamperometry was performed based on the potentiostatic intermittent titration technique (PITT) to minimize Ohmic contributions as the steady-state current is reached at each step. The tests were done using various potential step sizes with a duration of 120 s per step to ensure equilibrium. For a typical measurement (for a step size of 20 mV), the working electrode was initially equilibrated at 0.3 V vs.

Hg/Hg_2SO_4, and a series of cathodic steps (ΔE = –20 mV) were applied until reaching a lower cutoff voltage at −0.8 V vs. Hg/Hg_2SO_4. Then, a reverse process was applied until reaching an upper cutoff voltage at 0.3 V (anodic steps: ΔE = +20 mV). The resulting current was recorded as a function of time during each potential step. To reconstruct cyclic voltammograms at different equivalent scan rates (v), the mean current (i_{avg}) was determined by integrating the response current over a specific time window (e.g., the mean current of the first 1 s of each potential step) according to: $i_{avg} = \frac{\int_0^{\Delta t} i\, dt}{\Delta t}$ (where Δt = selected time and i = response current).[2,3]

Mechanistic studies

For *ex situ* analyses, Ti foil was used as the current collector for FT-IR and XPS measurements. For *ex situ* SEM, MGL280 carbon paper was used as the current collector. The *ex situ* electrodes contained 70 wt% active material, 20 wt% Ketjen black and 10 wt% PVDF, unless otherwise stated. Self-standing electrodes (0.2 mm thick) containing HATAQ active material, Ketjen black and poly(tetrafluoroethylene) (PTFE) in the weight ratio of 7:2:1 were used for *ex situ* PXRD investigation. The electrode mixture was combined together by using ethanol. For *ex situ* ^{1}H solid-state NMR measurements, the electrode mixture (HATAQ : Cu : PVDF = 3:6:1) was coated onto Ti current collector and cycled with a rate of 200 mA g^{-1}. The electrodes were dried in vacuum overnight at 100 °C. For all the other *ex situ* measurements except for *ex situ* ^{1}H solid-state NMR, the electrodes were cycled to various states of charge with a rate of 1 A g^{-1}, and the cells were disassembled. The electrodes were washed with DI water and dried in vacuum at 100 °C overnight prior to the *ex situ* characterization.

Full cell measurements

The TCBQ cathodes were prepared by first mixing the active material and Ketjen black by mortar and pestle for 30 min. Then, the mixture and PTFE polymer binder (60 wt% dispersion in water) were added into isopropanol, and further sonicated for 1 h. The mass ratio between active material, conducting agent and binder is 5:4:1. After isopropanol was evaporated, the membrane was dried at 70 °C under vacuum overnight. The obtained membrane was then pressed onto a titanium mesh current collector with an active material mass loading of 5 mg cm^{-2}.

For full cell measurements, the cells were assembled by using HATAQ as anode and TCBQ as cathode. HATAQ electrode was prepared with a weight ratio of 7:2:1 for HATAQ : Ketjen black : PVDF using MGL280 carbon paper as the current collector. TCBQ electrode was prepared using a ratio of 5:4:1 (TCBQ : Ketjen black : PTFE) using Ti mesh as the current collector. The mass ratio of the negative to positive active

material (N/P ratio) was kept at approximately 1:2.5. The HATAQ and TCBQ electrodes were individually pre-activated by charging and discharging for 5 cycles in three-electrode half-cells assembled by using platinum foil counter electrode and Hg/Hg_2SO_4 reference electrode. After pre-activation, three-electrode full cells were then assembled with HATAQ electrode (fully discharged state, at –0.5 V, with constant voltage held at the end of preactivation), TCBQ electrode (fully charged state, at 0.5 V, with constant voltage held at the end of preactivation) and Hg/Hg_2SO_4 reference electrode using 4 M H_2SO_4 aqueous electrolyte. The capacity of the full cell was calculated based on the HATAQ anode.

Results

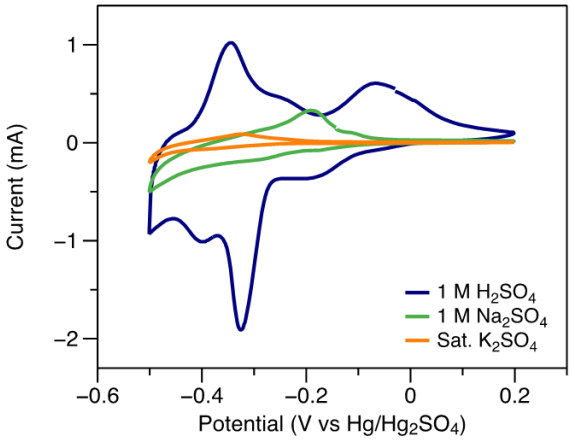

Fig. S1 CV plots of HATAQ at 1 mV s^{-1} in different aqueous electrolytes, 1 M H_2SO_4, 1 M Na_2SO_4 and saturated K_2SO_4.

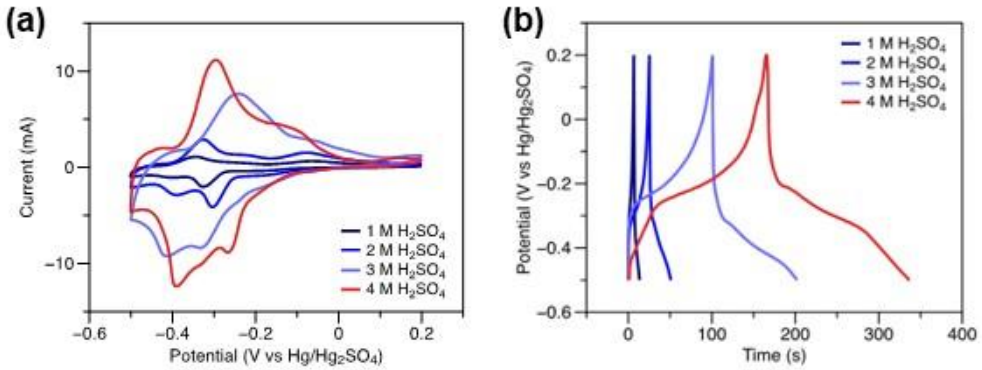

Fig. S2 (a) CV plots of HATAQ in different concentrations of H_2SO_4 aqueous electrolytes at a scan rate of 1 mV s^{-1}. (b) Galvanostatic discharge/charge plots from H_2SO_4 aqueous electrolytes, 1 to 4 M concentrations at a current density of 1 A g^{-1}.

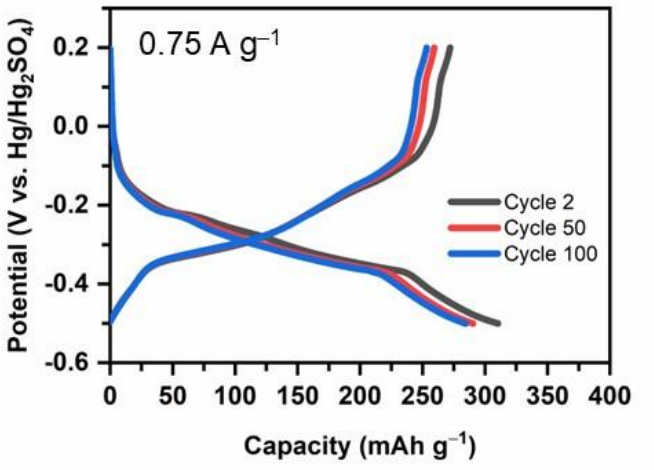

Fig. S3 Voltage profiles of HATAQ in 4 M H_2SO_4 aqueous electrolyte at 0.75 A g^{-1}.

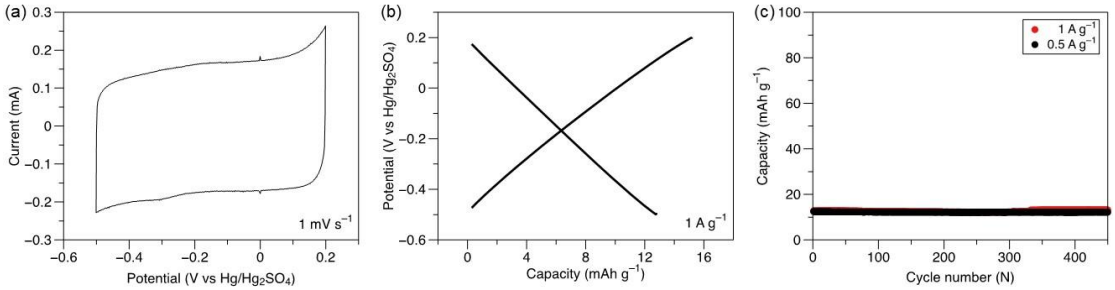

Fig. S4 Electrochemical properties of the conductive carbon (electrode ratio: Ketjen black : PVDF = 9:1) in 4 M H_2SO_4 aqueous electrolyte: (a) CV plot at scan rate of 1 mV s^{-1}. (b) Voltage profile at current density of 1 A g^{-1}. (c) Capacity retention plots at 0.5 A g^{-1} (black) and 1 A g^{-1} (red). The delivered capacity of Ketjen black at this electrode ratio is estimated to be ~13 mAh g^{-1} (between –0.5 V and 0.2 V). At rates higher than 1 A g^{-1}, the capacity contribution from Ketjen black is considered to be almost negligible within this voltage window.

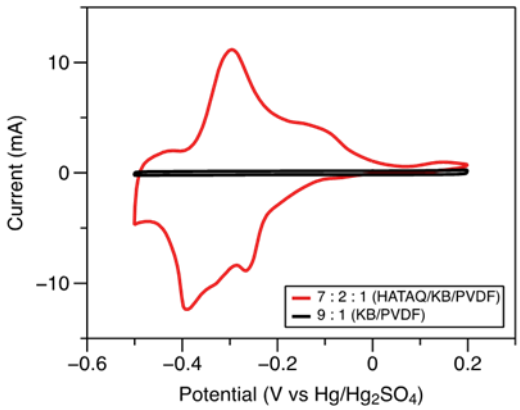

Fig. S5 Cyclic voltammogram of HATAQ plotted together with that of Ketjen black electrode in 4 M H_2SO_4 aqueous electrolyte at a scan rate of 1 mV s^{-1}.

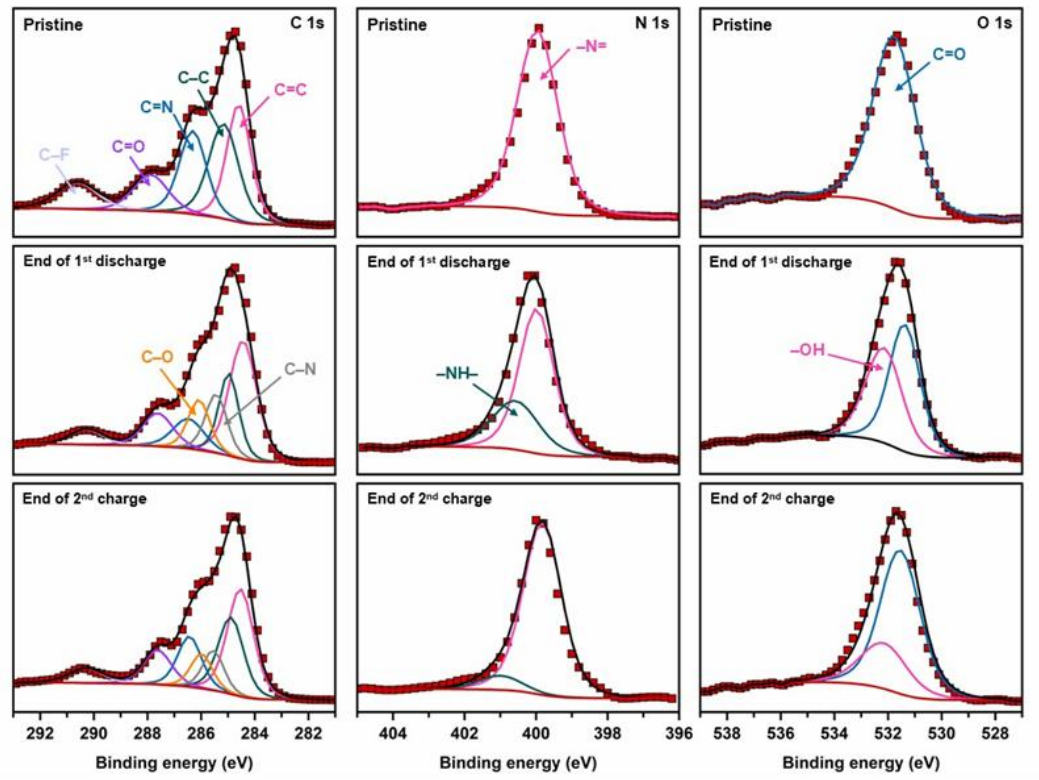

Fig. S6 Deconvolution of the high-resolution XPS spectra of HATAQ electrodes cycled at 1 A g^{-1}: pristine state, end of discharge and end of charge (C 1s (Left); O 1s (Middle); N 1s (Right)).

Activation energy calculation

The activation energy for charge transfer (E_a) is calculated based on the Arrhenius equation:

$\ln(R_{ct}^{-1}) = -E_a/RT + C$

where C is constant, R is gas constant and T is temperature. The charge transfer resistance (R_{ct}) was obtained by fitting Nyquist plots from EIS with a typical equivalent circuit.

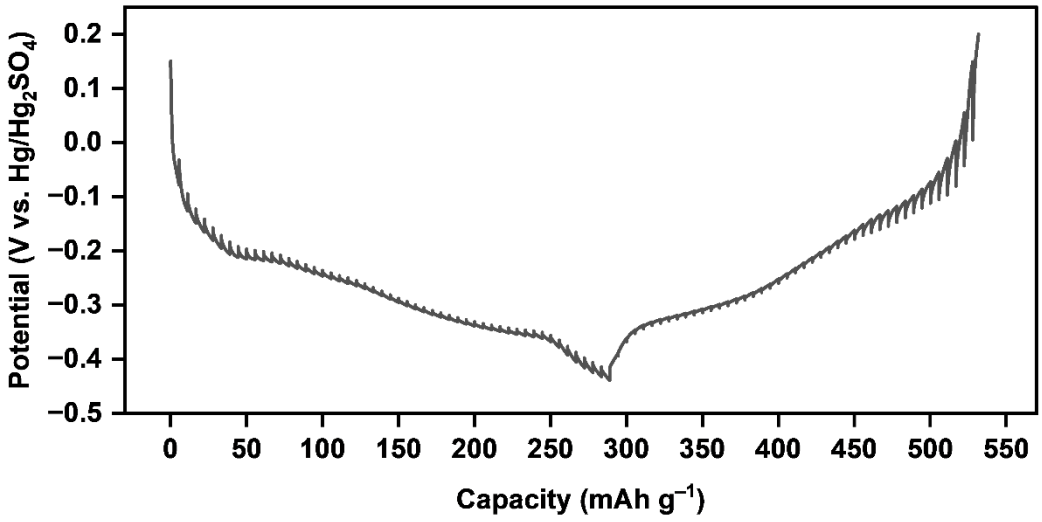

Fig. S7 GITT curve of HATAQ electrode at 1 A g^{-1}.

Determination of ionic diffusion coefficients by GITT

The ionic diffusion coefficients (*D*) were calculated using the GITT method based on Fick's second law of diffusion, according to the following equation:[4,5]

$$D = \frac{4}{\pi\tau}\left(\frac{mV_M}{MA}\right)^2\left(\frac{\Delta E_S}{\Delta E_\tau}\right)^2$$

where τ represents the pulse time (s), m is the mass of active material (g), V_M is the molar volume of electrode material ($cm^3\ mol^{-1}$), M is the molecular weight of electrode material ($g\ mol^{-1}$), A is the area of electrode-electrolyte interface, ΔE_τ is the transient potential caused by current pulse and ΔE_S is the stable potential resulting from relaxation after discharging/charging.

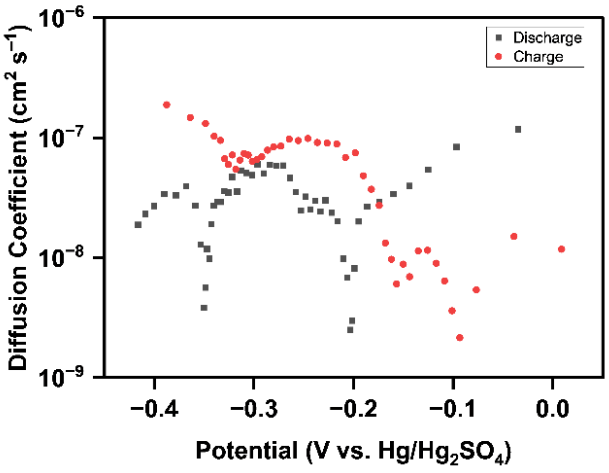

Fig. S8 Ionic diffusion coefficients calculated from the GITT curve of HATAQ.

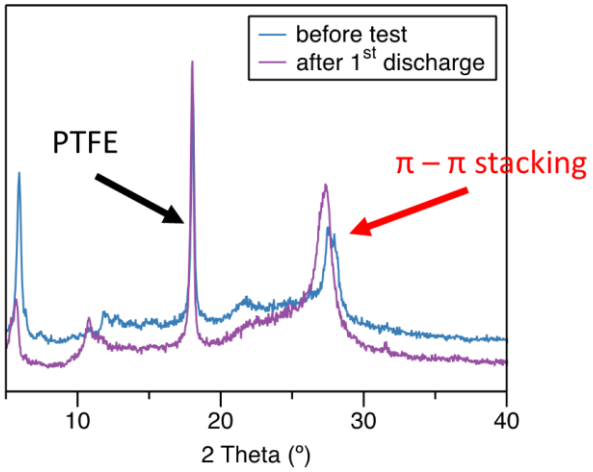

Fig. S9 PXRD pattern of pristine HATAQ electrode and that of discharged electrode with an obvious peak shift from 28.0 to 27.5º, indicating an expansion of π–π distance during discharge presumably due to proton insertion.

Density functional theory (DFT) calculations

Theoretical analysis of sequential protonation in HATAQ. To keep track of how protons are distributed between N and carbonyl O sites during protonation, we introduced the notation

$$\mathrm{HATAQH}_n^{(k_N,k_O)}$$

where:

n– total number of added protons and electrons,

k_N– number of protons bound to N sites (N–H),

k_O– number of protons bound to O sites (O–H)

and $k_N + k_O = n$.

For example, initial state $\mathrm{HATAQ} = \mathrm{HATAQH}_0^{(0,0)}$, N-protonated is $\mathrm{HATAQH}_1^{(1,0)}$ and O-protonated species: $\mathrm{HATAQH}_1^{(0,1)}$, etc.

First protonation (n = 1). For the first protonation transfer step, we evaluated the tautomeric equilibrium between the two possible mono-protonated species:

$$\mathrm{HATAQH}_1^{(1,0)} \rightleftharpoons \mathrm{HATAQH}_1^{(0,1)}$$

DFT calculations at TPSS/def2-SVP level of theory show that the N-protonated tautomer is lower in Gibbs free energy by 4.72 kcal/mol. This energy difference is sufficiently large to establish a clear preference for protonation at the N rather than at the carbonyl O in the initial protonation step.

For clarity, we use the term "protonation" to describe each step, while noting that the underlying process is a proton-coupled electron-transfer event in which a proton and an electron are added simultaneously.

Second protonation (n = 2). Here, we look at the three types of proton distributions at fixed $\mathrm{n} = 2$:

$$\mathrm{HATAQH}_2^{(2,0)} \rightleftharpoons \mathrm{HATAQH}_2^{(1,1)} \rightleftharpoons \mathrm{HATAQH}_2^{(0,2)}$$

$\mathrm{HATAQH}_2^{(2,0)}$– both protons on N, with ΔΔG = 0.0 kcal/mol,

$\mathrm{HATAQH}_2^{(1,1)}$– one N–H and one O–H, with ΔΔG = 11.6 kcal/mol,

$\mathrm{HATAQH}_2^{(0,2)}$ – both protons on O, with ΔΔG = 7.2 kcal/mol.

All relative energies are obtained at the TPSS/def2-SVP level. These results show that the all-N protonated species is strongly favored over both mixed (N–H/O–H) and all-O protonation structures. The energy separation is substantial, both O-protonated patterns lie > 7.0 kcal/mol above the fully N-protonated form; therefore, at n = 2, the system continues to protonate exclusively at the N sites.

Third protonation (n = 3). For the third protonation step, we focus on the most relevant competition, i.e., continued protonation at N versus the protonation at carbonyl

O. We start from the lowest energy 2N state, $\mathrm{HATAQH}_2^{(2,0)}$, and compare the two 3H tautomer products:

$$(3)\mathrm{HATAQH}_3^{(3,0)} \rightleftharpoons \mathrm{HATAQH}_3^{(2,1)}$$

$\mathrm{HATAQH}_3^{(3,0)}$ is more stable by 4.5 kcal/mol at TPSS/def2-SVP level relative to $\mathrm{HATAQH}_3^{(2,1)}$. This result indicates that protonation continues to favor N sites.

Charge evolution during progressive protonation. Since the energetic analysis for n = 1–3 indicates a persistent preference for N-protonation, we model higher protonation states under the assumption that all six N sites are filled before protonation shifts to the carbonyl O atoms. To assess whether this sequential N-first → O-later picture is chemically reasonable, we examined how the electronic environment of the remaining (non-protonated) heteroatoms evolves along the $\mathrm{HATAQH}_n^{(k_N,k_O)}$ series using Hirshfeld charges.

Hirshfeld charge analysis shows that, as protons and electrons are added, the unprotonated N and O atoms become progressively more electron-rich (Fig. S10). For the nitrogens, analysis is possible up to n = 5, beyond which all N atoms are protonated. Over this range, the average Hirshfeld charge on unprotonated N shifts from about q = −0.121 at 0H to q = −0.146 at 5H, with the small fluctuations attributed to local resonance. A similar trend is observed for carbonyl oxygens, the average charge on unprotonated O evolves from ≈ −0.277 at 0H to ≈ −0.433 at 11H, after which all O atoms possess protons. This increased delocalization of positive charge over the conjugated framework rationalizes why the N-protonated tautomers are systematically lower in free energy than their O-protonated counterparts in the present calculations. Moreover, the preference for N over O protonation in HATAQ is consistent with previous DFT/NBO analysis on this molecule in Zn–HATAQ cells, where N-protonation was shown to generate a resonance-stabilized vinylogous amide whereas O-protonation leads to a less delocalized phenolic tautomer.[6]

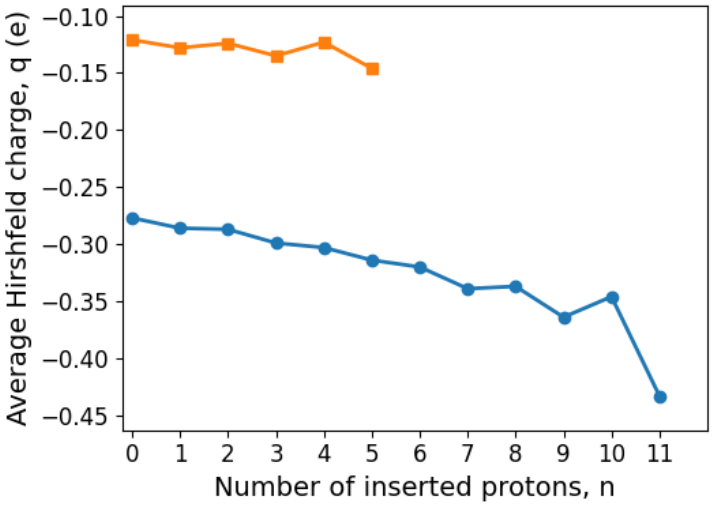

Fig. S10 Averaged Hirshfeld charges on the unprotonated N and O atoms (orange and blue, respectively) in the $HATAQH_n$ species.

Overall, the increased electron density on the remaining heteroatoms indicates that progressive reduction enhances their basicity, maintaining a strong thermodynamic driving force for further protonation.

Final protonation (up to n = 12). For each step $n = 1–12$, we computed the Gibbs free energy of proton/electron addition:

$$HATAQH_{n-1} + H^+ + e^- \rightarrow HATAQH_n$$

The resulting free-energy profile (Table S1) fluctuates between approximately −49 and −57 kcal/mol across the full insertion series. These values are not intended to represent quantitative redox potentials; rather, they confirm that none of the twelve protonation events introduces a destabilizing barrier or disrupts the overall progression. The small oscillations in ΔG primarily arise from changes in electronic multiplicity (singlet vs doublet) and local geometric relaxation, particularly adjustments in hydrogen-bonding patterns, rather than any intrinsic instability of the protonated intermediates.

Table S1. Absolute electronic and Gibbs free energies for sequential protonation of $HATAQH_n$ series.

Species	ΔE, kcal/mol	ΔG, kcal/mol
$HATAQH_1$	-71.1	-58.4
$HATAQH_2$	-78.5	-64.8
$HATAQH_3$	-71.5	-58.7
$HATAQH_4$	-73.3	-58.3
$HATAQH_5$	-68.2	-54.3
$HATAQH_6$	-73.2	-57.6
$HATAQH_7$	-58.6	-46.1
$HATAQH_8$	-66.1	-53.0
$HATAQH_9$	-57.2	-45.7
$HATAQH_{10}$	-64.2	-51.8
$HATAQH_{11}$	-58.7	-45.6
$HATAQH_{12}$	-62.1	-49.0

To obtain a more chemically intuitive picture, we recalculated the same series in terms of addition of hydrogen using molecular hydrogen as the reference:

$$HATAQH_{n-2} + H_2 \rightarrow HATAQH_n$$

The corresponding reaction free energies are summarized in Fig. S11 and Table S2. In this representation, the driving force for each H_2-addition step is more moderate and gradually decreases in magnitude as protonation proceeds, consistent with progressive occupation of the available redox-active sites. Importantly, even the final H_2-addition step remains exergonic at the molecular DFT level, suggesting that highly protonated HATAQ species are thermodynamically accessible in principle.

Expressed in terms of reduction potentials, the calculated trend is also broadly consistent with experiment. The first two-electron step (0→2H) gives a calculated potential of −0.25 V vs Hg/Hg_2SO_4, close to the experimental cathodic peak at −0.26 V. The second step (2→4H) gives −0.40 V, in good agreement with the peak at −0.39 V. The third step (4→6H) is calculated at −0.48 V, which lies near the negative boundary of the experimental working window (−0.50 V). Subsequent steps beyond 6H are calculated below approximately −0.60 V and therefore are expected to be difficult to access electrochemically under the present conditions, even if they remain thermodynamically favorable in the isolated-molecule DFT description.

This analysis provides a plausible explanation for the experimentally observed capacity, corresponding to approximately 6–7 electron equivalents. The first three two-electron steps account for six electrons within the accessible potential range, whereas the next step appears to lie near the edge of the working window and may therefore be only partially utilized. In this picture, the more highly protonated states (8–12H) are formally accessible in the molecular thermodynamic sense, but are not expected to

contribute substantially under the present electrochemical conditions because they require more negative potentials.

Table S2. Calculated electronic and Gibbs free-energy changes and derived reduction potentials for formal H_2 addition in the $HATAQH_n$ series.

Species	ΔE, kcal/mol	ΔG, kcal/mol	E vs SHE, V	E vs Hg/Hg_2SO_4, V
$HATAQH_2$	-32.9	-18.6	0.404	-0.246
$HATAQH_4$	-27.4	-11.8	0.255	-0.395
$HATAQH_6$	-25.1	-7.7	0.167	-0.483
$HATAQH_8$	-15.6	-2.0	0.043	-0.607
$HATAQH_{10}$	-14.2	-2.3	0.051	-0.600
$HATAQH_{12}$	-14.9	-0.7	0.016	-0.634

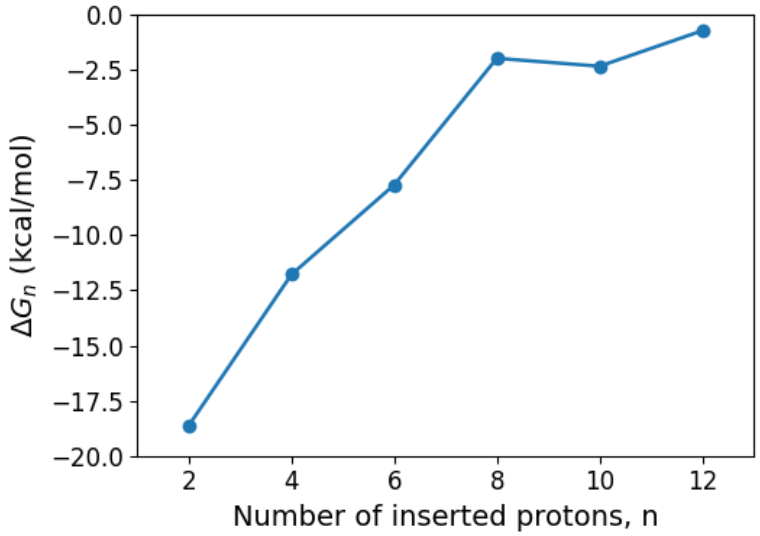

Fig. S11 Absolute electronic and Gibbs free energies for sequential H_2 addition in the $HATAQH_n$ series.

Taken together, these results suggest the following overall picture:

- Steps 1–6. Protonation is favored initially at N sites, consistent with the energetic preference observed for the early stages (n = 1–3).
- Steps 7–12. After the N sites are occupied, subsequent protonation is expected to involve O-containing sites, which become increasingly competitive as the electronic structure evolves along the reduction sequence.
- Energetic continuity. The absence of any strongly unfavorable thermodynamic step suggests that the HATAQ framework can, in principle, support the full $12H^+/12e^-$ redox sequence at the molecular level, although only part of this manifold is expected to be accessible within the experimental potential window.

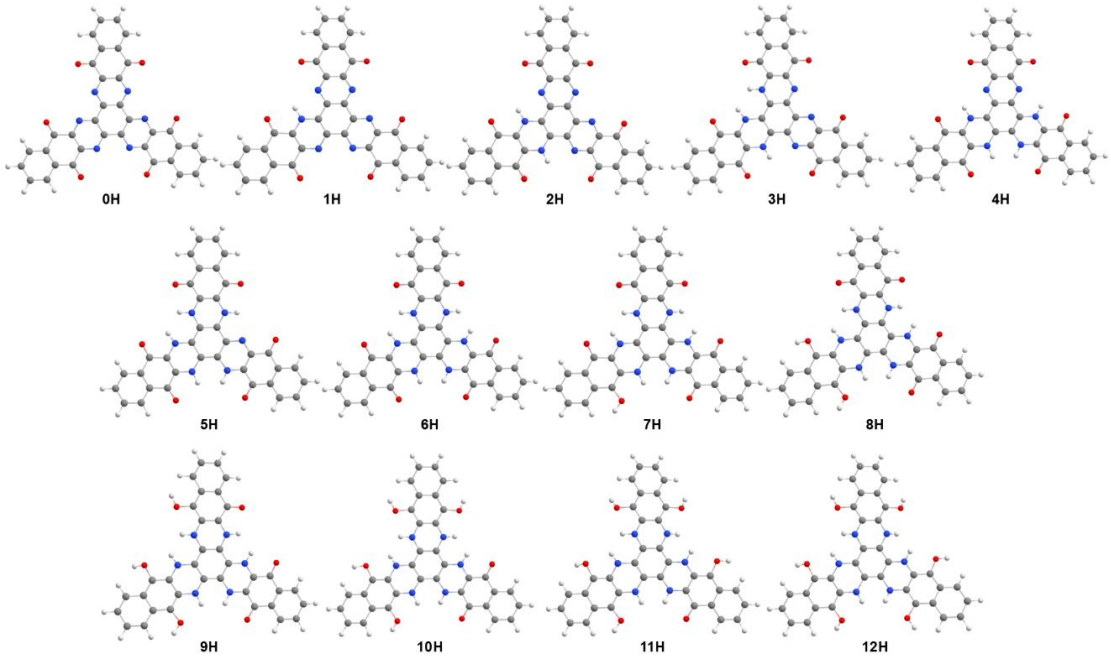

Fig. S12 Optimized molecular structures of $HATAQH_n$ (n = 0–12).

Overall, the DFT results provide a thermodynamic framework for understanding the formal 12-electron proton-coupled redox manifold of HATAQ, while also offering a qualitative explanation for why only approximately 6–7 electron equivalents are realized experimentally within the accessible aqueous electrochemical window.

Comparison with HATN: role of the quinone 'arms' in protonation thermodynamics.

To examine the role of the carbonyl-containing 'arms' in HATAQ, we carried out an analogous set of calculations on hexaazatriphenylene (HATN, chemical structure in Table S4), which preserves the same number of imine-like N sites on a related aza-aromatic core but lacks the quinone C=O groups. This comparison provides a useful reference for evaluating how extension of the conjugated framework and incorporation of carbonyl functionality affect the thermodynamics of proton-coupled reduction.

Table S3 summarizes the calculated two-electron-averaged reduction potentials for the N-site protonation sequence of HATN (TPSSh/def2-TZVP, H_2 reference). Across all three N-protonation pairs, the HATN potentials are shifted to more negative values than those of HATAQ. For HATN, the first pair (0→2H) is calculated at approximately −0.43 V vs Hg/Hg_2SO_4, whereas the second and third pairs are shifted further negative to about −0.66 and −0.73 V. In contrast, the first three corresponding HATAQ pairs are calculated within or near the experimental working window. These results suggest that a larger fraction of the N-site proton-coupled redox manifold is

electrochemically accessible in HATAQ than in HATN under comparable aqueous conditions.

Table S3. Calculated two-electron-averaged reduction potentials for HATN. Potentials are calculated for the reaction $HATN_{n-2} + H_2 \rightarrow HATN_n$ at the TPSSh/def2-TZVP level.

Species	ΔE, kcal/mol	ΔG, kcal/mol	E vs Hg/Hg_2SO_4, V
$HATN_2$	-25.2	-10.1	-0.430
$HATN_4$	-14.0	+0.3	-0.657
$HATN_6$	-9.4	+3.8	-0.734

The difference between the two systems is consistent with their distinct electronic structures. In the stepwise protonation sequence, the odd-numbered intermediates correspond to open-shell states, whereas the even-numbered states are closed-shell. In the more compact HATN framework, accommodation of the odd-electron intermediates appears less favorable, which contributes to the more negative reduction potentials. In HATAQ, extension of the π-conjugated system together with the presence of carbonyl-containing arms provides additional opportunities for charge and spin delocalization, thereby stabilizing the reduced protonated states. This effect is likely an important factor in bringing the early proton-coupled reduction steps of HATAQ into a more accessible potential range.

Importantly, the HOMO–LUMO gaps of neutral HATAQ (3.04 eV) and HATN (3.06 eV) are essentially identical, indicating comparable intrinsic semiconducting character. Since both electrodes also rely on a conductive carbon network for electronic transport, the superior electrochemical performance of HATAQ is more naturally attributed to its protonation thermodynamics and hydrogen-bond-assisted proton transport pathways than to differences in electronic conductivity.

The calculated trend is also qualitatively consistent with the experimentally reported electrochemical behavior of HATN-based electrodes, which show lower practical accessibility of the full theoretical redox manifold than would be expected for an ideal six-electron process.

Beyond redox thermodynamics, the structural comparison also suggests a difference in the local environments available for proton motion. In crystalline HATAQ, neighboring molecules are arranged such that carbonyl and imine sites can participate in extended hydrogen-bond-assisted contacts after protonation, providing a plausible framework for local proton transfer between adjacent redox-active groups. HATN lacks the carbonyl oxygen acceptors present in HATAQ and therefore cannot support an analogous O-containing hydrogen-bond network. This structural difference

is consistent with the idea that HATAQ may better support local hydrogen-bond-assisted proton transfer in the solid state.

Taken together, the HATN comparison supports the view that the quinone-containing extension in HATAQ does more than simply add extra O-based protonation sites. It also shifts the early N-site proton-coupled reduction steps to more accessible potentials and provides a solid-state environment more compatible with hydrogen-bond-assisted local proton transfer.

Periodic crystal structure response to progressive protonation. After establishing the molecular-level protonation sequence, we examined the corresponding response of the crystalline solid by optimizing the periodic structures of HATAQ, $HATAQH_6$, and $HATAQH_{12}$ using VASP (Fig. S13). The purpose of this analysis was to determine whether progressive proton insertion would induce major structural disruption in the solid state.

Across all three compositions, the overall aromatic framework remains largely planar, and no bond breaking, collapse of the layered motif, or loss of recognizable π-stacking is observed. Instead, protonation leads mainly to localized and chemically intuitive adjustments. At intermediate protonation ($HATAQH_6$), the newly formed N-H groups participate in additional intra- and interlayer hydrogen-bonding interactions, accompanied by modest out-of-plane displacements that accommodate these contacts while preserving the layered packing. At higher protonation ($HATAQH_{12}$), the structure remains clearly recognizable, with a more developed hydrogen-bonding network but with the conjugated backbone and stacked arrangement still retained.

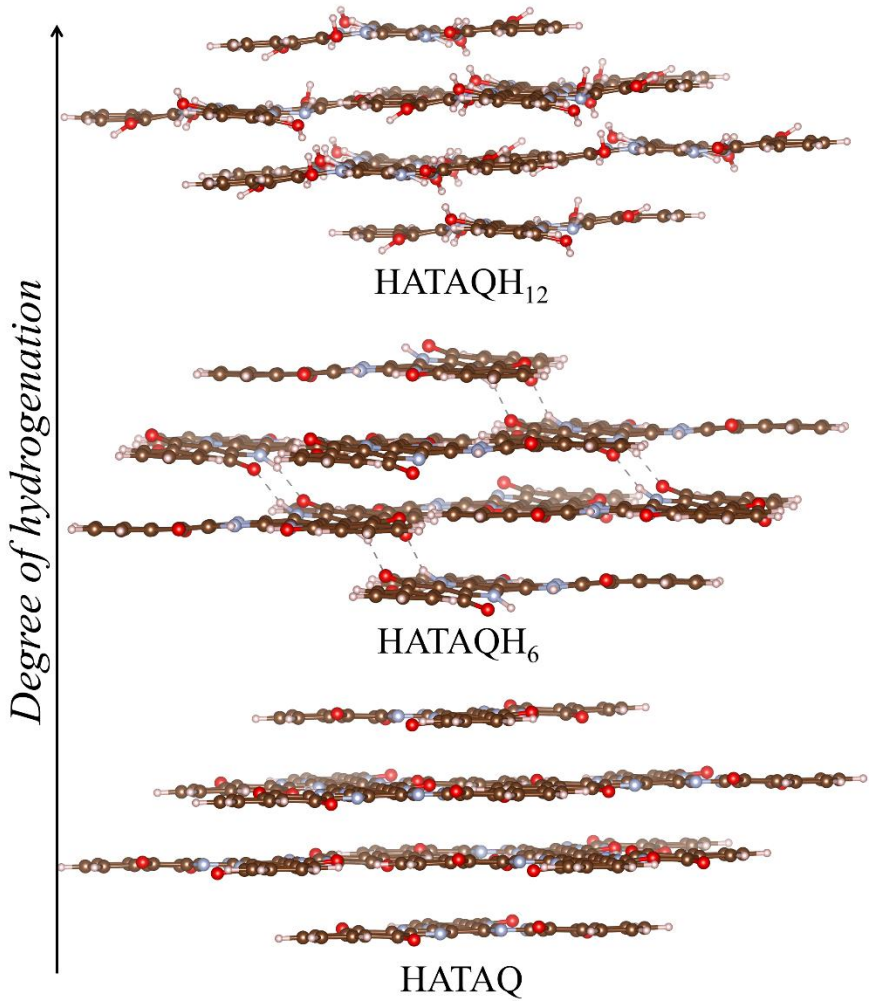

Fig. S13 Structural evolution of HATAQ upon progressive protonation – HATAQ, $HATAQH_6$, and $HATAQH_{12}$.

Overall, the periodic DFT results indicate that deep protonation primarily reorganizes local hydrogen-bonding interactions rather than disrupting the conjugated framework itself. This structural robustness is consistent with the experimentally observed reversibility and extended cycling stability.

The 13th protonation step. To probe the upper limit of proton accommodation beyond the canonical 12-site N/O protonation manifold, we considered addition of one extra proton to the fully protonated state. In this context, the 13th protonation step should be viewed as a limiting-case structural test rather than as a claim about the dominant electrochemical process under operating conditions. We modeled the reaction

$$\mathrm{HATAQH}_{12}^{(6,6)} + \mathrm{H_3O^+} \longrightarrow \mathrm{HATAQH}_{13}^{(7,6)} + \mathrm{H_2O}$$

At the molecular level, this reaction is thermodynamically favorable, with a computed ΔG = –9.3 kcal/mol, indicating that formation of $HATAQH_{13}$ is thermodynamically accessible in this isolated-molecule model. Periodic optimization

of the corresponding $HATAQ_{13}$ crystal further shows that the framework remains intact: the layers undergo moderate lateral sliding and slight bending, but the overall stacked structure is preserved without collapse or severe disorder (Fig. S14).

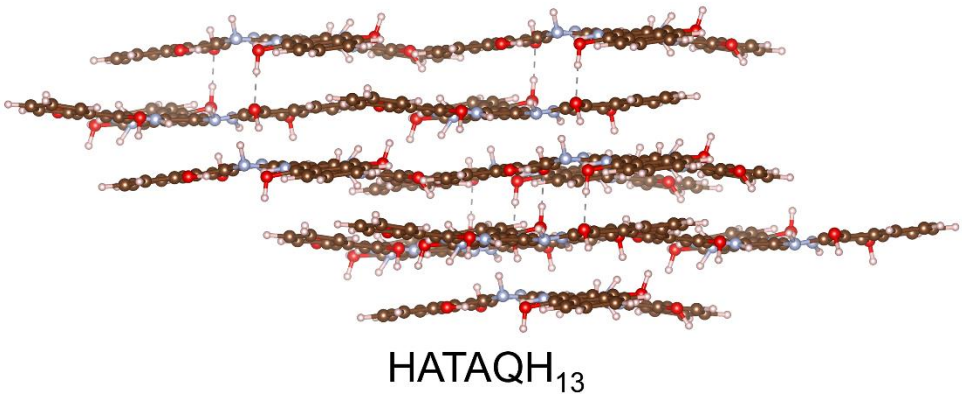

Fig. S14 Periodic structure of $HATAQH_{13}$.

These results suggest that the HATAQ lattice retains substantial structural flexibility even under an extreme protonation load and the crystal framework remains structurally coherent.

Proton transfer leading to the 13th protonation state. To obtain a qualitative estimate of the energetic cost of local proton transfer in a strongly protonated environment, we used the optimized $HATAQH_{13}$ structure as a starting point and modeled a representative proton-transfer event. A cluster containing several neighboring HATAQ molecules was extracted from the periodic structure. The carbon atoms were fixed at their crystallographic positions, while H, N, and O atoms were allowed to relax. Within this constrained framework, the motion of the additional proton was followed from its initial N-bound position toward a nearby carbonyl O atom along a pre-existing N-H···O hydrogen bond (Fig. S15).

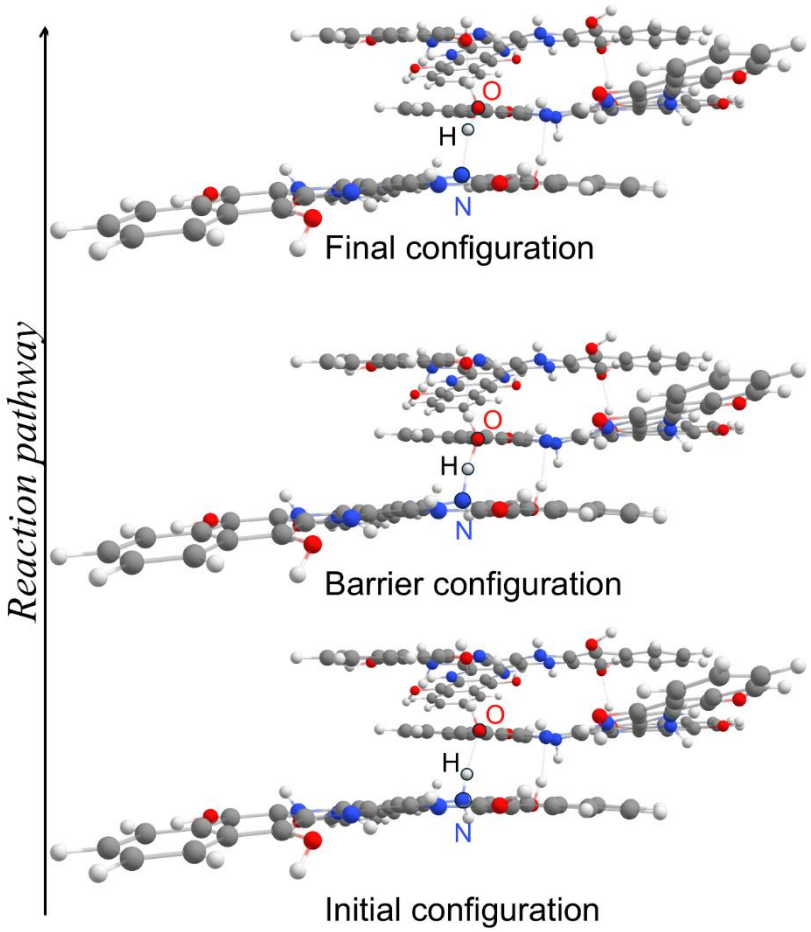

Fig. S15. Model proton-transfer pathway in the HATAQ-13H cluster.

Because a full transition-state search for such a constrained multi-molecule cluster would be computationally cumbersome and of limited added reliability, we instead carried out a relaxed one-dimensional scan along the N···H···O coordinate and used the local maximum on this profile as an approximate barrier estimate. The resulting barrier is about 9 kcal/mol.

This value is close in magnitude to the activation energy extracted experimentally for charge-transfer-related kinetics (0.353 eV ≈ 8.1kcal/mol). Given the simplified and highly constrained nature of the model, this level of agreement should be regarded as qualitative. Nevertheless, it is consistent with the view that hydrogen-bond-assisted local proton transfer in the solid state can occur on an energetically reasonable scale and may contribute to the observed electrochemical behavior.

Taken together, the periodic and cluster calculations support a unified picture in which HATAQ combines (i) thermodynamically accessible early proton-coupled redox steps within the experimental window, (ii) substantial structural tolerance toward deep protonation, and (iii) a solid-state arrangement capable of supporting local hydrogen-bond-assisted proton transfer.

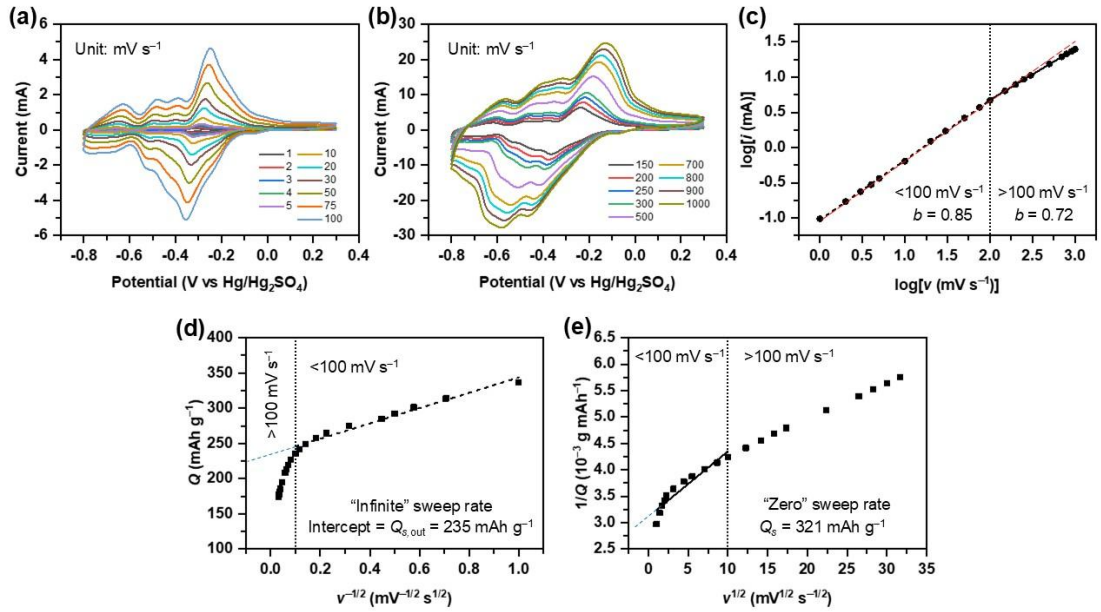

Fig. S16 (a) CV plots at scan rates of 1–100 mV s^{-1}. (b) CV plots at scan rates of 150–1000 mV s^{-1}. (c) Plot of log(scan rate) vs. log(peak current) following a power law described by $i = av^b$, showing a significantly larger slope of 0.85 below 100 mV s^{-1} and a smaller slope of 0.72 above 100 mV s^{-1}. (d) Plot of Q as a function of $v^{-1/2}$, with extrapolation to $v = \infty$ to estimate the "outer" surface contribution ($Q_{s,out}$) of HATAQ. (e) Plot of Q^{-1} as a function of $v^{1/2}$, with extrapolation to $v = 0$ to estimate the total charge from the surface-controlled contribution (Q_s).

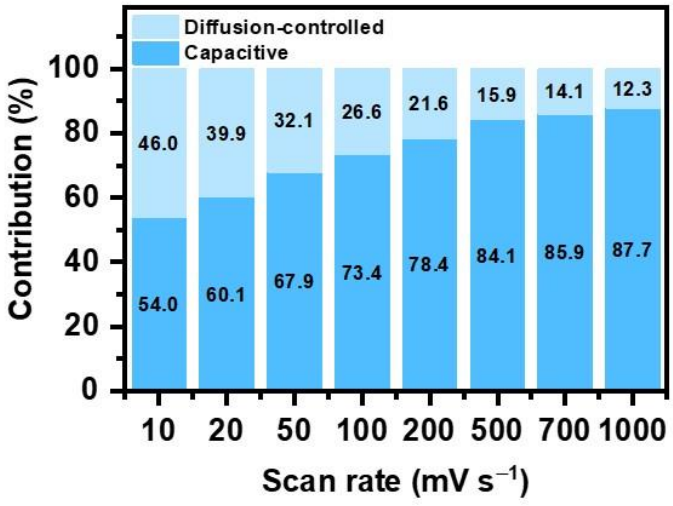

Fig. S17 Capacity contributions at different sweep rates of HATAQ calculated according to $i(V) = k_1 v + k_2 v^{1/2}$.

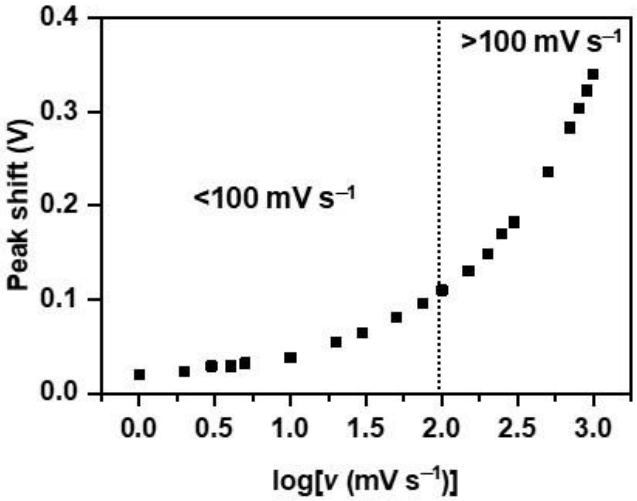

Fig. S18 Peak shifts of the main redox couple as a function of log(sweep rate). The cathodic/anodic peak separation is found to be less than 0.1 V and increases slowly with the sweep rate, indicating surface-limited redox behaviour, while at high scan rates (above a critical rate of 100 mV s^{-1}), the peak shift increases much more dramatically as the system reaches diffusion-limited behaviour. It is worth noting that cathodic/anodic peak separation is usually greater than 0.1 V even at a scan rate as low as 0.1 mV s^{-1}, when intercalation kinetics are at play in battery materials.[7]

Kinetic studies

Q in Fig. S16 is calculated from the CV data. For each scan rate, Q is calculated using the following equation:

$$Q = \frac{A}{2(3.6)\mathrm{m}v}$$

where m is mass of active material and v is scan rate. A is CV plot area obtained by integrating the current response during potential sweep.[7]

In this work, to investigate the charge storage kinetics of HATAQ and demonstrate its pseudocapacitive bahaviour, CV measurements were performed at scan rates of 1–1000 mV s^{-1} (Fig. S16a and S16b) and several analyses were done. First, we used a simple relationship between the applied sweep rate (v) and observed electrochemical current (i) to determine the presence of surface-controlled/capacitive (vs. semi-infinite diffusion-controlled) kinetics (Fig. S16c). This analysis, also known as b-value analysis, is a very common first-line tool to analyze the kinetic behavior of battery materials: $i(V) = \mathrm{a}v^b$, where i is the current at a specific potential (V), a and b are adjustable parameters, and b is the slope of the linear fit of the log i vs. log v for various sweep rates.[8] When the current is directly proportional to the sweep rate, b = 1, the process is

surface-controlled. When b = 0.5, the reaction is semi-infinite diffusion-controlled. When the *b*-value falls between 0.5 and 1, the mechanism can be attributed to mixed control (a linear combination of diffusion and capacitive contributions).[3,9] As shown in Fig S16c, from the lowest rate of 1 to 100 mV s^{-1}, the b value is 0.85, indicating dominantly surface-controlled behavior. Above 100 mV s^{-1}, the slope drops to 0.72, implying kinetic limitation arising from diffusion constraints.

Under the mixed control assumption, a linear combination of surface- and diffusion-controlled currents was proposed: $i(V) = k_1 v + k_2 v^{1/2}$, where $k_1 v$ and $k_2 v^{1/2}$ terms correspond to capacitive and diffusion-limited effects.[3,10] Dunn et al. utilized this concept to deconvolute capacitive vs. diffusive contributions to the total current by rearranging to $i(V)/v^{1/2} = k_1 v^{1/2} + k_2$ and plotting $v^{1/2}$ vs. $i(V)/v^{1/2}$. k_1 and k_2 are derived from the slope and the *y*-axis intercept, respectively, at specific potentials across various scan rates.[11–13] The charge stored due to surface- and diffusion-controlled current contributions of HATAQ can then be quantified at different sweep rates, as seen in Fig. S17 below. The *b*-value analysis and k_1, k_2 analysis are methods to interpret current responses (measured directly from electrochemical characterization techniques), which are very common for battery electrode materials. However, one major limitation of these approaches is that they do not account for the shift of potential with higher sweep rates due to increased Ohmic losses,[3] which become significant at high sweep rates (>100 mV/s in this work, as shown in the peak shift plot below, Fig. S18). Even though these equations are simplistic, they still can provide a critical and quantifiable understanding of how the electrode materials possess pseudocapacitive features.

Trasatti et al. developed a method based on voltammetric charge to deconvolute the "inner" (less accessible) and "outer" (more accessible) surface contributions.[14,15] In this method, it is assumed that the voltammetric charge (Q) can be divided into surface-controlled and diffusion-controlled contributions (Q_s and Q_d) so that $Q = Q_s + Q_d$. The surface-controlled component can then be further divided into the "inner" surface contribution, ($Q_{s,in}$) and "outer" surface contribution ($Q_{s,out}$): $Q_s = Q_{s,in} + Q_{s,out}$. The "inner" surface contribution is assumed to be sweep rate dependent (due to lower accessibility of redox sites) and the "outer" surface contribution is invariant of sweep rates.[7,14]

Therefore, $Q_s = \begin{cases} Qs, \text{out} & \text{when } v = \infty \\ Qs, in + Qs, out & \text{when } v = 0 \end{cases}$

With these boundary conditions, $Q_{s,in}$ and $Q_{s,out}$ can be extrapolated by plotting the charge as a function of sweep rate. Assuming semi-infinite linear diffusion and a linear relationship between Q_d and $v^{-1/2}$, $Q = Q_s + Q_d$ can be rearranged into $Q = Q_{s,out} + A_1 v^{-1/2}$ (where A_1 is a constant) when $v = \infty$. By plotting Q vs. $v^{-1/2}$ (Fig. S16d),

$Q_{s,out}$ can be determined from the *y*-intercept ($v^{-1/2} = 0$; or $v = \infty$) of the linear extrapolation, which is estimated to be 235 mAh g^{-1}. This value of $Q_{s,out}$ indicates the "outer" surface contribution, which is more easily accessible by the electrolyte.[3,15,16]

For $Q_{s,in}$, we can obtain the value when $v = 0$. Assuming that Q^{-1} decreases linearly with $v^{1/2}$, $Q = Q_s + Q_d$ can be rearranged into $Q^{-1} = Q_s^{-1} + A_2 v^{1/2}$ (where A_2 is a constant). By plotting Q^{-1} vs. $v^{1/2}$ (Fig. S16e), Q_s^{-1} can be determined from the *y*-intercept ($v^{1/2} = 0$) of the linear extrapolation to be 3.11 x 10^{-3} g mAh^{-1} or Q_s = 321 mAh g^{-1}.[3,15,16] This total charge from the surface-controlled contribution, combining both the "inner" surface contribution ($Q_{s,in}$) which is relatively less accessible and "outer" surface contribution ($Q_{s,out}$) which is more accessible, can then be used to calculate $Q_{s,in}$. By further determining the $Q_{s,out}/Q_s$ ratio ($Q_{s,out}/Q_s$ = 235 mAh g^{-1}/321 mAh g^{-1} = 0.73), we can conclude that approximately 73% of the total charge of HATAQ corresponds to the charge from "outer" surface contribution, which is easily accessible by the electrolyte during surface redox processes.[7,14] These results are in good agreement with the high rate capability observed in Fig. 3 (main text), which can be supported primarily by the rapid surface-level redox activities. Even though this method does not account for Ohmic losses (similarly to the *b*-value and k_1, k_2 analyses), it is assumed to be valid in a certain reliability range, which minimizes the contribution of Ohmic drop factor.[16]

To address the redox peak potential shifts due to polarization, which becomes significant at really high sweep rates (>100 mV s^{-1}), we also performed multiple-step chronoamperometry based on PITT to mitigate the impact of Ohmic drop.[2,3] Fig. S19 shows the experimental cyclic voltammograms compared with the reconstructed cyclic voltammograms from PITT at sweep rates of 1 to 1000 mV s^{-1}.

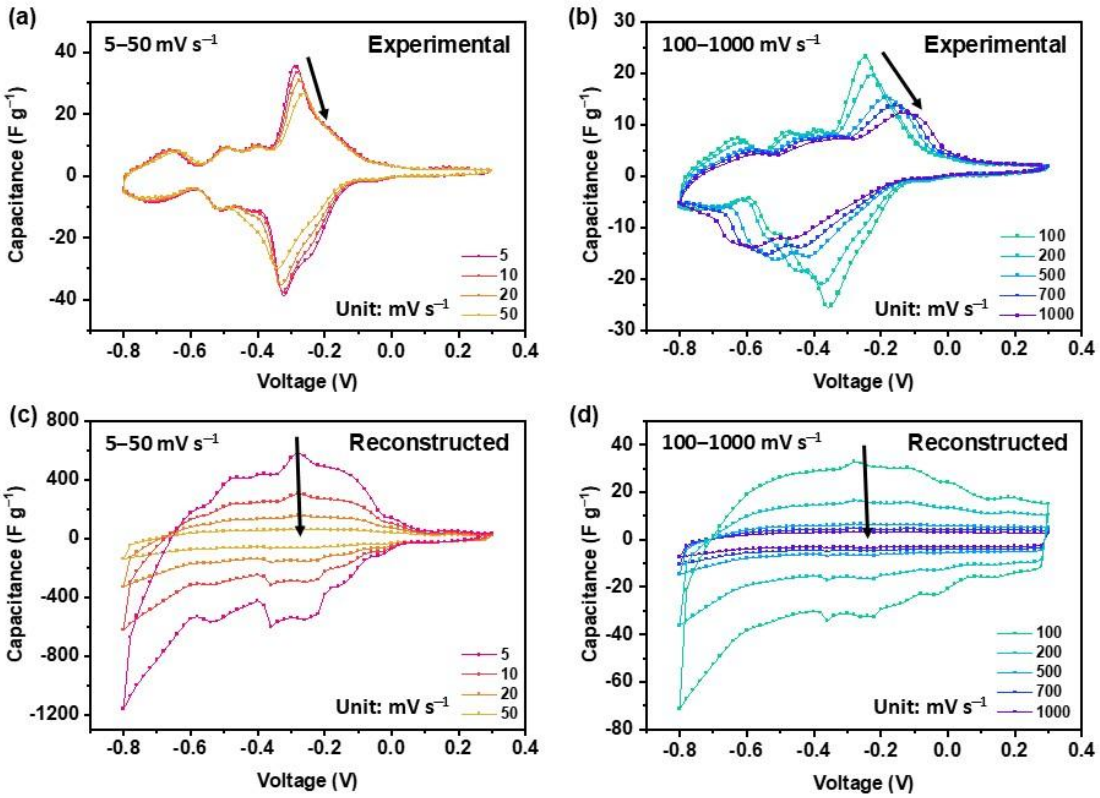

Fig. S19 (a) and (b) Experimental cyclic voltammograms of HATAQ for sweep rates of 5–50 and 100–1000 mV s^{-1}, respectively. (c) and (d) Reconstructed cyclic voltammograms from multiple-step chronoamperometry measurements (based on PITT) at 5–50 and 100–1000 mV s^{-1}, respectively.

The fact that the significant peak shift is only witnessed when the sweep rate is 100 mV s^{-1} or above reveals pseudocapacitive nature of HATAQ in the proton battery system, and explains the exceptional rate performance. Overall, the pseudocapacitive electrode materials are found to be kinetically limited at low rates only by the speed of the surface-level Faradaic reactions, which is surface controlled, whereas at higher rates they are limited by electrolyte diffusion.[3,7]

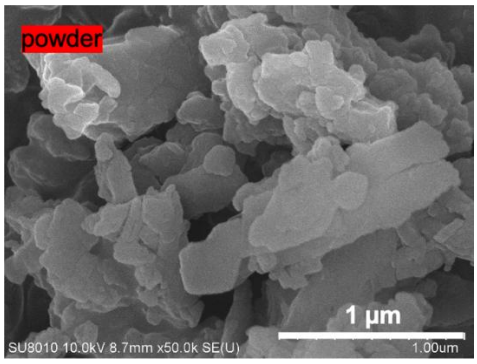

Fig. S20 SEM image of as-synthesized HATAQ powder.

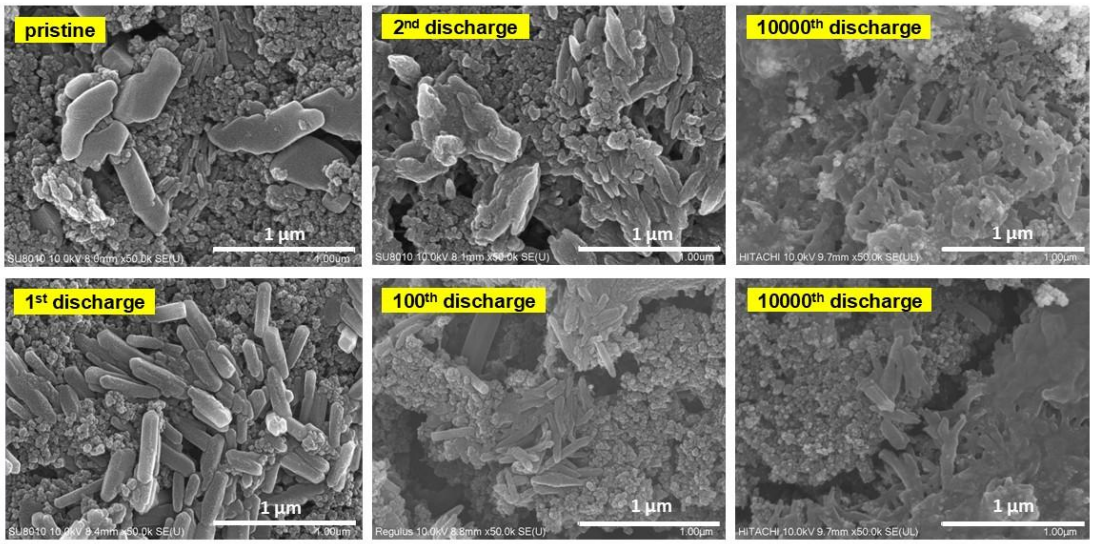

Fig. S21 SEM images of *ex situ* HATAQ electrodes at different states of charge (compared to the pristine electrode) up to 10000 cycles.

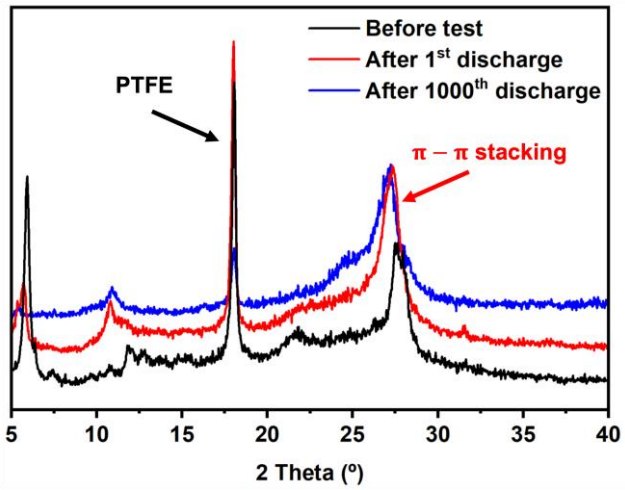

Fig. S22 PXRD pattern of HATAQ electrode after 1000 cycles showing no obvious change compared with that from the 1st cycle, thus suggesting that the HATAQ superstructure remains stable throughout long-term cycling.

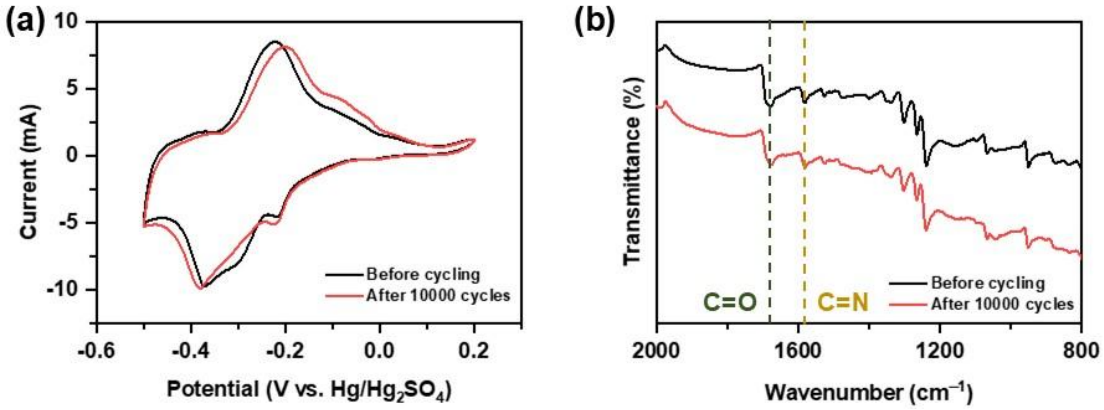

Fig. S23 (a) CV curves of HATAQ electrode before and after 10000 cycles. (b) FT-IR spectra of HATAQ electrode before and after 10000 cycles.

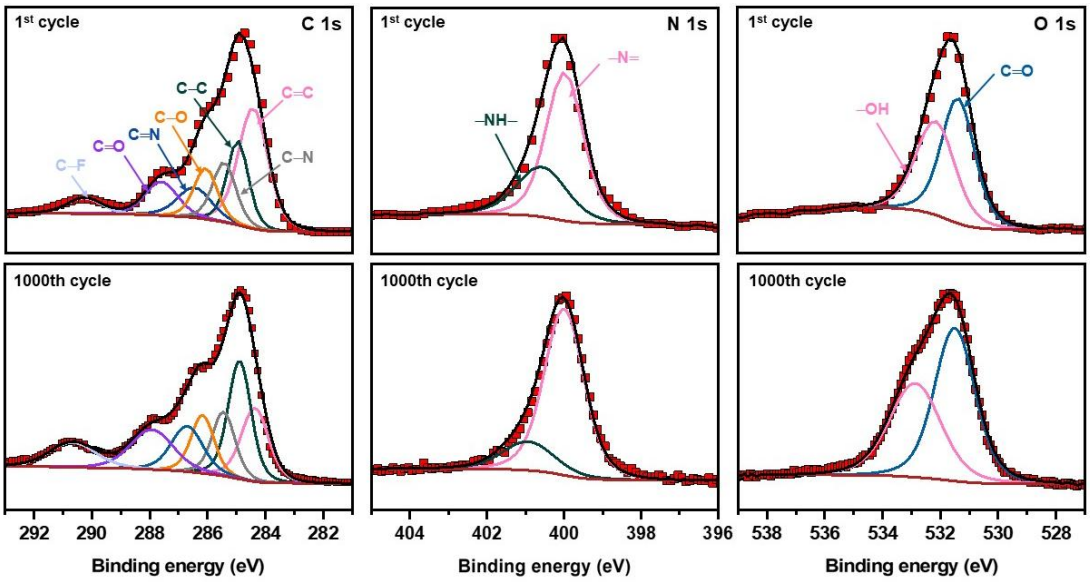

Fig. S24 Deconvolution of the high-resolution XPS spectra of HATAQ electrodes cycled at 1 A g^{-1} after 1000 cycles: C 1s (Left); N 1s (Middle); O 1s (Right).

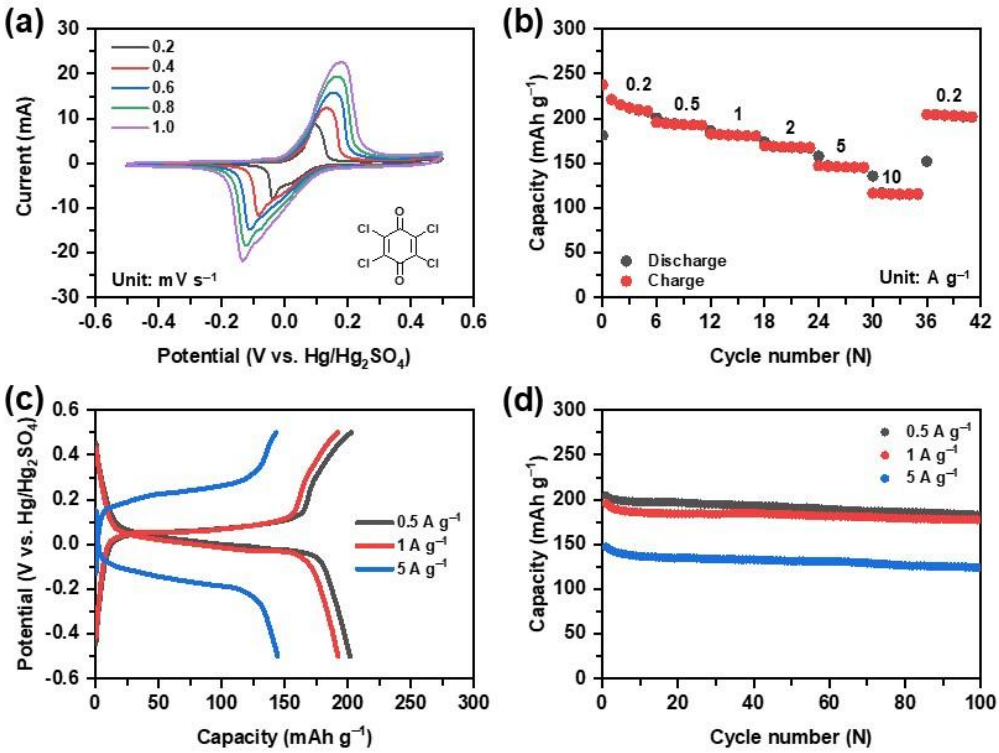

Fig. S25 (a) CV curves of TCBQ electrode with 4 M H_2SO_4 electrolyte at various scan rates of 0.2 – 1.0 mV s^{-1}. Inset shows the structure of TCBQ. (b) Rate capability of TCBQ electrode at various current densities ranging from 0.2 to 10 A g^{-1} with an initial capacity of ~220 mAh g^{-1} and capacity retention of 93% when returning to 1 A g^{-1}. (c) Galvanostatic discharge/charge profiles of TCBQ electrode at different current densities of 0.5, 1 and 5 A g^{-1}. (d) Capacity retention at current densities of 0.5, 1 and 5 A g^{-1}, with delivered initial capacities of 204, 195 and 147 mAh g^{-1} corresponding to retention of 89, 91 and 84 %, respectively.

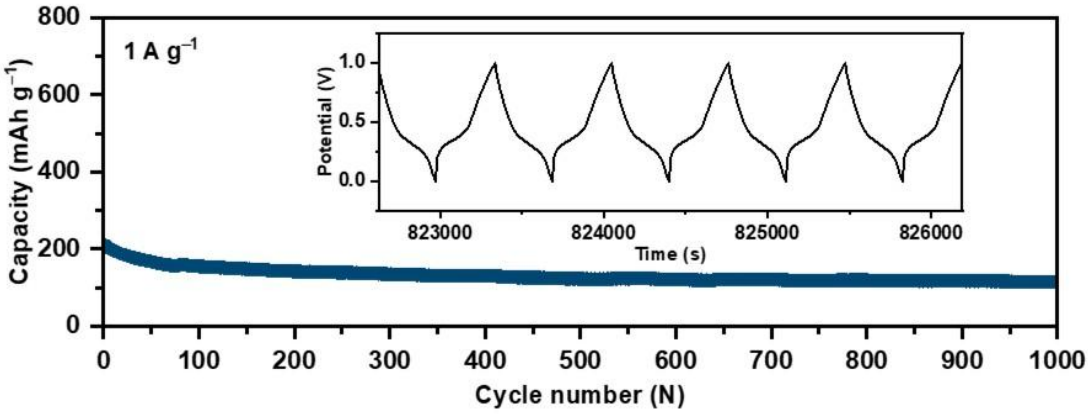

Fig. S26 Capacity retention plot of HATAQ/TCBQ full cell at 1 A g^{-1} for 1000 cycles with inset showing highly reversible voltage profiles.

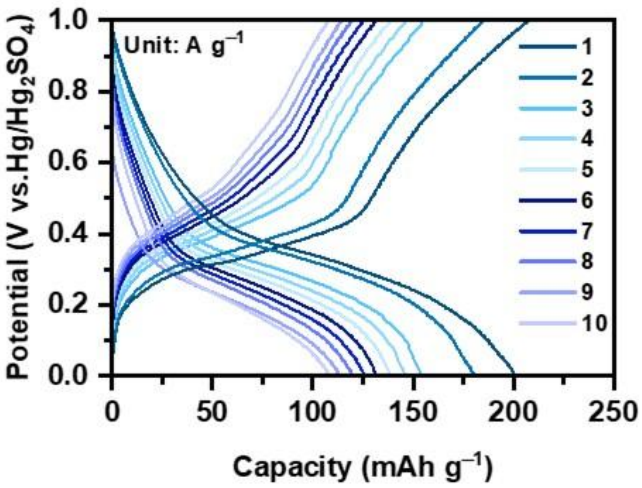

Fig. S27 Discharge/charge profiles of HATAQ/TCBQ full cells at current densities of 1−10 A g^{-1}.

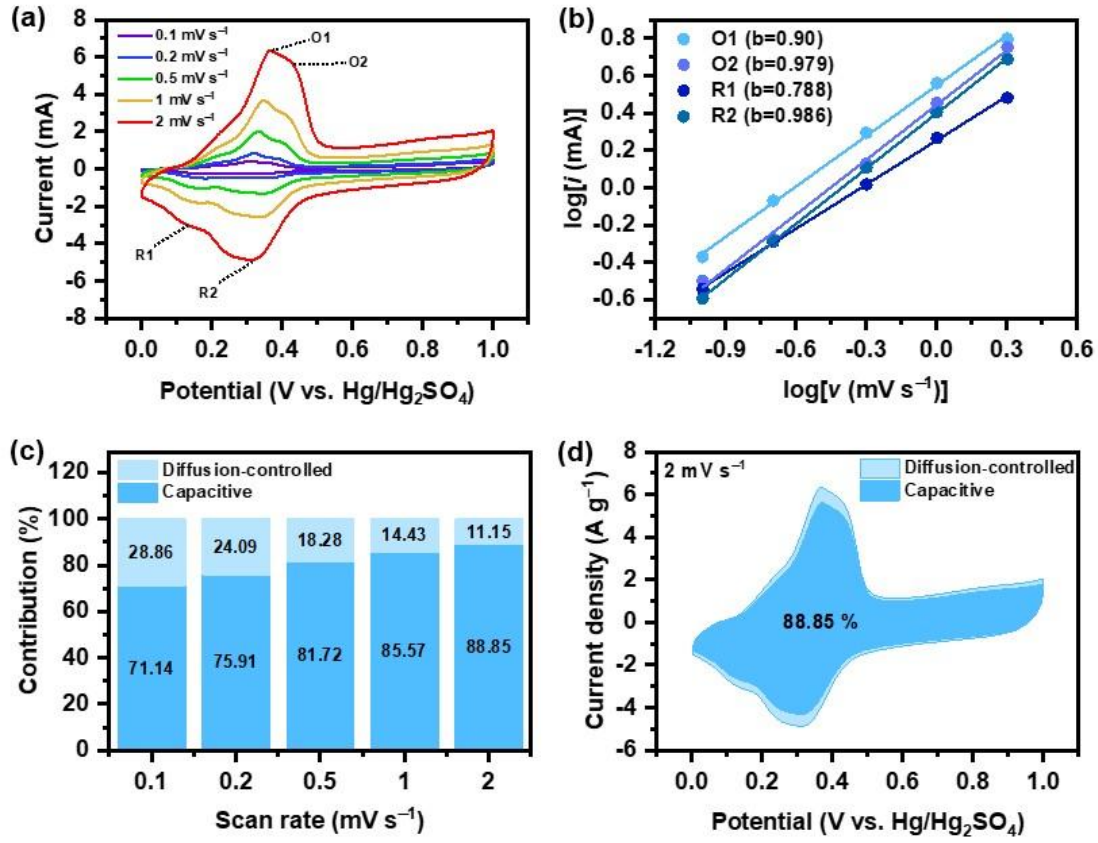

Fig. S28 CV analysis of HATAQ/TCBQ full cell at scan rates of 0.1–2 mV s^{-1}: (a) CV curves at various scan rates. (b) Relationship between log i (peak current) and log v (scan rate) from the CV curves in (a). The analysis of charge storage process was performed on HATAQ/TCBQ full cell with b values calculated from $i = av^b$. According to these results, the Faradaic charge storage associated with the peak maxima in CV has a significant capacitive contribution: b = 0.5 indicating traditional diffusion dominated charge storage, while b = 1 indicating capacitor-like charge storage. (c) Capacity contributions at different scan rates calculated according to $i = k_1v + k_2v^{1/2}$. (d) Cyclic voltammogram at 2 mV s^{-1}, showing the contribution from capacitive process up to 88.85%, in good agreement with the fast kinetics of proton–coupled electron transfer reactions in aqueous-based HATAQ/TCBQ full cell.

Table S4. Organic-based electrode materials for aqueous proton batteries reported in the literature.

Structure	Composition of Electrode (active material: conductive carbon: binder)	Electrolyte (Mass Loading)	Theoretical Capacity (Electron Transfer)	Voltage Window (V)	Initial Capacity at Lowest Rate Reported	Reversible Capacity at Highest Rate Reported	Capacity Retention at Highest Rate	Ref.
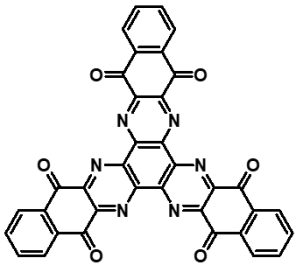	**HATAQ**: Ketjen black (KB): polyvinylidene fluoride (PVDF) (7:2:1)	4 M H_2SO_4 (2–3 mg cm^{-2})	516 mAh g^{-1} (12 e^-)	–0.5–0.2 V vs. Hg/Hg_2SO_4 [–0.11–0.59 V vs. Ag/AgCl]	310 mAh g^{-1} at 0.75 A g^{-1}	140 mAh g^{-1} at 20 A g^{-1}	91% after 1000 cycles and 90% after 10000 cycles at 20 A g^{-1}	This work
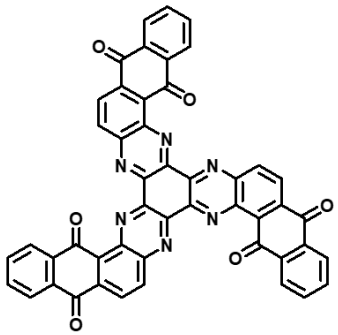	**PZQN**: acetylene black: binder (7:2:1)	4 M H_2SO_4 (1.15 mg cm^{-2})	415 mAh g^{-1} (12 e^-)	–0.2–0.9 V vs. Ag/AgCl	263 mAh g^{-1} at 2 A g^{-1}	107 mAh g^{-1} at 40 A g^{-1}	90% after 16000 cycles at 10 A g^{-1}	17

Structure	Composition of Electrode (active material: conductive carbon: binder)	Electrolyte (Mass Loading)	Theoretical Capacity (Electron Transfer)	Voltage Window (V)	Initial Capacity at Lowest Rate Reported	Reversible Capacity at Highest Rate Reported	Capacity Retention at Highest Rate	Ref.
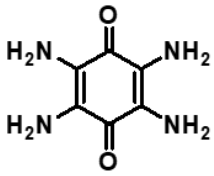	**TABQ**: KB: polytetrafluoroethylene (PTFE) (5:4:1)	0.5 M H_2SO_4 (6–8 mg cm^{-2})	319 mAh g^{-1} (2 e^-)	–0.4–0.55 V* vs. SCE [–0.42–0.53 V vs. Ag/AgCl]	307 mAh g^{-1} at 1 A g^{-1}	127 mAh g^{-1} at 20 A g^{-1}	62% after 5000 cycles at 5 A g^{-1}	18
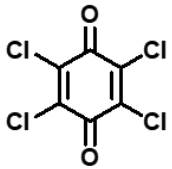	N/A	5 M H_2SO_4 (1 mg cm^{-2})	218 mAh g^{-1} (2 e^-)	0.2–0.8 V vs. Ag/AgCl	216 mAh g^{-1} at 0.1 A g^{-1}	62 mAh g^{-1} at 100 A g^{-1}*	~60% after 3000 cycles at 10 A g^{-1}	19
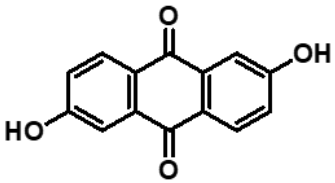	**DHAQ**: carbon black: PVDF (8:1:1)	1 M H_2SO_4 (3 mg cm^{-2})	110 mAh g^{-1} (1 e^-)	–0.6–0.6 V vs. Ag/AgCl	100 mAh g^{-1} at 1.7 A g^{-1}	51 mAh g^{-1} at 6.7 A g^{-1}	63% after 100 cycles at 6 A g^{-1}	20

Structure	Composition of Electrode (active material: conductive carbon: binder)	Electrolyte (Mass Loading)	Theoretical Capacity (Electron Transfer)	Voltage Window (V)	Initial Capacity at Lowest Rate Reported	Reversible Capacity at Highest Rate Reported	Capacity Retention at Highest Rate	Ref.
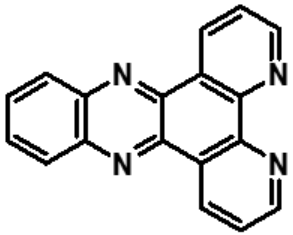	**DPPZ**: KB: Nafion ionomer (5 wt%, 75 µL) ~(2:2:3)	0.05 M H_2SO_4 (0.085 mg cm^{-2})	189 mA h g^{-1} (2 e^-)	−0.4–0.2 V vs. SCE [–0.42–0.18 V vs. Ag/AgCl]	102 mA h g^{-1} at 2 A g^{-1}	97 mA h g^{-1} at 15 A g^{-1}	~100% after 400 cycles at 6 A g^{-1}	21
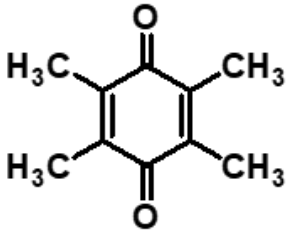	**TMBQ**: CNTs: PTFE (5:4:1)	0.5 M H_2SO_4 + 1 M $MnSO_4$	326 mAh g^{-1} (2 e^-)	–0.2–0.7 V* vs. Ag/AgCl	300 mAh g^{-1} at 1C (326 mA g^{-1})	177 mAh g^{-1} at 100C (32.6 A g^{-1})	N/A	22

Structure	Composition of Electrode (active material: conductive carbon: binder)	Electrolyte (Mass Loading)	Theoretical Capacity (Electron Transfer)	Voltage Window (V)	Initial Capacity at Lowest Rate Reported	Reversible Capacity at Highest Rate Reported	Capacity Retention at Highest Rate	Ref.
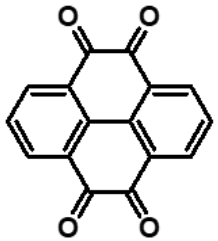	**PTO**: KB: PTFE (5:4:1)	4.2 M H_2SO_4 ($2\ mg\ cm^{-2}$)	400 mAh g^{-1} ($4\ e^-$)	0−6.5 V* vs. SCE [–0.02–6.48 V vs. Ag/AgCl]	376 mAh g^{-1} at 0.05 A g^{-1}	103 mAh g^{-1} at 50 A g^{-1}	74% after 5000 cycles at 2 A g^{-1}	23
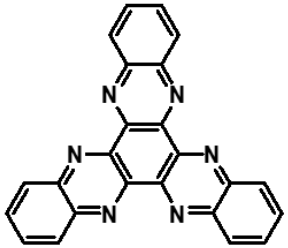	**HATN**: KB: PVDF (6:3:1)	0.05 M H_2SO_4 and 0.2 M $MnSO_4$ ($1.33\ mg\ cm^{-2}$)	418 mAh g^{-1} ($6\ e^-$)	−0.2–0.3 V* vs. Ag/AgCl	225 mAh g^{-1} at 1 A g^{-1}	134 mAh g^{-1} at 20 A g^{-1}	~100% after 2000 cycles at 1 A g^{-1}	24

Structure	Composition of Electrode (active material: conductive carbon: binder)	Electrolyte (Mass Loading)	Theoretical Capacity (Electron Transfer)	Voltage Window (V)	Initial Capacity at Lowest Rate Reported	Reversible Capacity at Highest Rate Reported	Capacity Retention at Highest Rate	Ref.
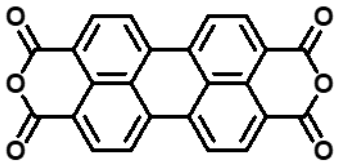	**PTCDA**: C-45: PVDF (7:2:1)	1 M H_2SO_4 (2 mg cm^{-2})	68 mAh g^{-1} (1 e^-)	−0.55–0 V vs. Ag/AgCl	85 mAh g^{-1} at 1 A g^{-1}	N/A	~68% after 120 cycles at 1 A g^{-1}	25
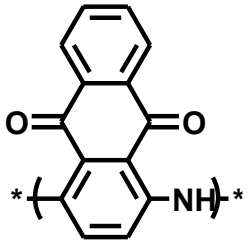	**PNAQ**: KB: PTFE (7:2:1)	4 M H_2SO_4 (1–2 mg cm^{-2})	240 mAh g^{-1} (2 e^-)	−0.25–0.1 V vs. Ag/AgCl	87.6 mAh g^{-1} at 1 A g^{-1}	71 mAh g^{-1} at 10 A g^{-1}	80% after 100 cycles at 1 A g^{-1}	26

Structure	Composition of Electrode (active material: conductive carbon: binder)	Electrolyte (Mass Loading)	Theoretical Capacity (Electron Transfer)	Voltage Window (V)	Initial Capacity at Lowest Rate Reported	Reversible Capacity at Highest Rate Reported	Capacity Retention at Highest Rate	Ref.
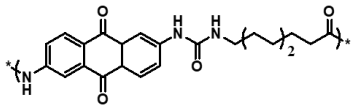	**PUQ**: acetylene black: PTFE (7:2:1)	0.5 M H_2SO_4 (1.5 mg cm^{-2})	135 mAh g^{-1} (2 e^-)	−0.4–0.2 V vs. Ag/AgCl	94 mAh g^{-1} at 1 A g^{-1}	66.5 mAh g^{-1} at 20 A g^{-1}	82% after 1000 cycles at 5 A g^{-1}	27
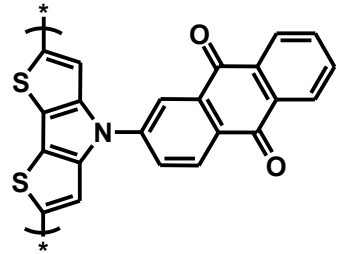	**pDTP-AQ**: acetylene black: PTFE (7:2:1)	1 M H_2SO_4 (1 mg cm^{-2})	208 mAh g^{-1} (3 e^-)	−0.4–0 V vs. Ag/AgCl	119 mAh g^{-1} at 5C (~1 A g^{-1})	~58.5 mAh g^{-1} at 50C (~10 A g^{-1})	83% after 1000 cycles at 10C (~2 A g^{-1})	28
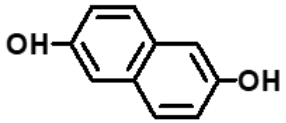	**2,6-DHNQ**: KB: PTFE (6:3:1)	0.5 M H_2SO_4 (1–2 mg cm^{-2})	335 mAh g^{-1} (2 e^-)	0–1.2 V vs. SCE [–0.02–1.18 V vs. Ag/AgCl]	91.6 mAh g^{-1} at 1 A g^{-1}	81.9 mAh g^{-1} at 20 A g^{-1}	80% after 1000 cycles at 5 A g^{-1}	29

Structure	Composition of Electrode (active material: conductive carbon: binder)	Electrolyte (Mass Loading)	Theoretical Capacity (Electron Transfer)	Voltage Window (V)	Initial Capacity at Lowest Rate Reported	Reversible Capacity at Highest Rate Reported	Capacity Retention at Highest Rate	Ref.
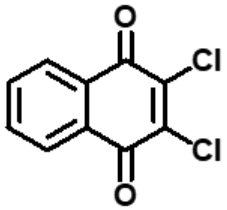	**2Cl-NQ**: acetylene black: PVDF (7:2:1)	1 M H_2SO_4 (1.9–2.6 mg cm^{-2})	236 mAh g^{-1} (2 e^-)	−0.6–0.2 V vs. Hg/Hg_2SO_4 [–0.21–0.59 V vs. Ag/AgCl]	~225 mAh g^{-1} at 1 A g^{-1}	198.3 mAh g^{-1} at 4 A g^{-1}	98.6% after 1800 cycles at 1 A g^{-1}	30
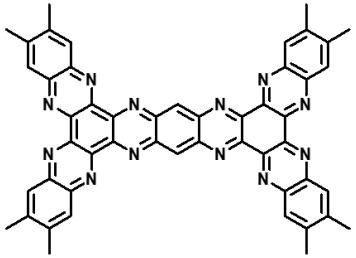	**PDQPZ**: acetylene black: PVDF (7:2:1)	1 M H_2SO_4	400 mAh g^{-1} (12 e^-)	−0.2–0.8 V vs. Ag/AgCl	205 mAh g^{-1} at 1 A g^{-1}	137 mAh g^{-1} at 22 A g^{-1}	91.1% after 10000 cycles at 15 A g^{-1}	31

Structure	Composition of Electrode (active material: conductive carbon: binder)	Electrolyte (Mass Loading)	Theoretical Capacity (Electron Transfer)	Voltage Window (V)	Initial Capacity at Lowest Rate Reported	Reversible Capacity at Highest Rate Reported	Capacity Retention at Highest Rate	Ref.
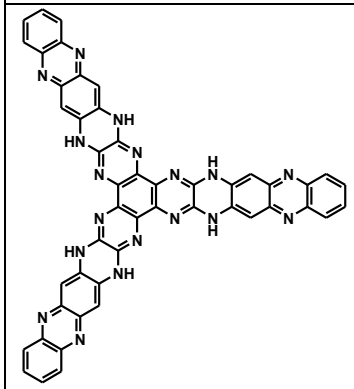	**DPHAT**: carbon black: PVDF (7:2:1)	1 M H_2SO_4 (1–2 mg cm^{-2})	377 mAh g^{-1} (12 e^-)*	−0.3–0.5 V vs. Ag/AgCl	207.9 mAh g^{-1} at 1 A g^{-1}	178.2 mAh g^{-1} at 10 A g^{-1}	91.8% after 10000 cycles at 5 A g^{-1} 93.6% after 3000 cycles at 10 A g^{-1}	32
MoO_3	**MoO_3**: super-P: PVDF (7:2:1)	9.5 m H_3PO_4	N/A	−0.5–0.3 V vs. Ag/AgCl	218 mAh g^{-1} at 1 A g^{-1}	140 mAh g^{-1} at 100 A g^{-1}	82% after 1000 cycles at 2 A g^{-1}	33

Structure	Composition of Electrode (active material: conductive carbon: binder)	Electrolyte (Mass Loading)	Theoretical Capacity (Electron Transfer)	Voltage Window (V)	Initial Capacity at Lowest Rate Reported	Reversible Capacity at Highest Rate Reported	Capacity Retention at Highest Rate	Ref.
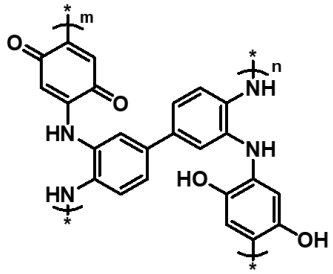	**PQANS**: acetylene black: PVDF (7:2:1)	2 M H_2SO_4 (1–2 mg cm^{-2})	253 mAh g^{-1} (4 e^-)*	−0.2–0.8 V vs. Ag/AgCl	162.8 mAh g^{-1} at 0.3 A g^{-1}*	66.8 mAh g^{-1} at 10 A g^{-1}	92% after 12000 cycles at 10 A g^{-1}	34
	**PIQ** (2 mg): KB (2 mg) Nafion ionomer (5 wt%, 75 µL)	3 M H_2SO_4 (0.084 mg cm^{-2})	401 mAh g^{-1} (10 e^-)	−0.15–0.97 V vs. SCE* [–0.17–0.95 V vs. Ag/AgCl]	255.6 mAh g^{-1} at 1 A g^{-1}	201 mAh g^{-1} at 20 A g^{-1}	~100% after 150 cycles at 10 A g^{-1}*	35

Structure	Composition of Electrode (active material: conductive carbon: binder)	Electrolyte (Mass Loading)	Theoretical Capacity (Electron Transfer)	Voltage Window (V)	Initial Capacity at Lowest Rate Reported	Reversible Capacity at Highest Rate Reported	Capacity Retention at Highest Rate	Ref.
DTT 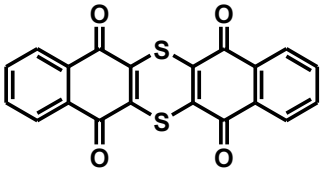	**DTT**: KB: PTFE (6:3:1)	2 M H_2SO_4 + 0.2 M $MnSO_4$ (3 mg cm^{-2})	285 mAh g^{-1} (3 e^-)	−0.2–0.6 V vs. Ag/AgCl	212 mAh g^{-1} at 0.05 A g^{-1}	100 mAh g^{-1} at 10 A g^{-1}	92% after 4000 cycles at 3 A g^{-1}	36
BPZT 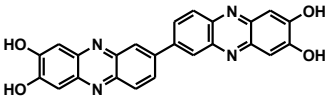	**BPZT**: KB: PTFE (6:3:1)	2 M H_2SO_4 (2 mg cm^{-2})	254 mAh g^{-1} (2 e^-)	−0.2–0.5 V vs. Ag/AgCl*	138 mAh g^{-1} at 0.2 A g^{-1}	97 mAh g^{-1} at 20 A g^{-1}	95% after 1000 cycles at 1 A g^{-1}	37

Structure	Composition of Electrode (active material: conductive carbon: binder)	Electrolyte (Mass Loading)	Theoretical Capacity (Electron Transfer)	Voltage Window (V)	Initial Capacity at Lowest Rate Reported	Reversible Capacity at Highest Rate Reported	Capacity Retention at Highest Rate	Ref.
HDC 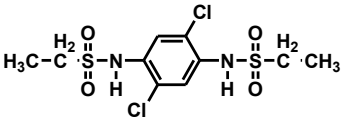	**HDC**: KB: CMC (7:2:1)	1 M H_2SO_4-PVA	148.4 mAh g^{-1} (2 e^-)	−0.76–1.9 V vs. Ag/AgCl	~103 mAh g^{-1} at 0.1 A g^{-1}	N/A	N/A	38
C_4N-50% MWCNT 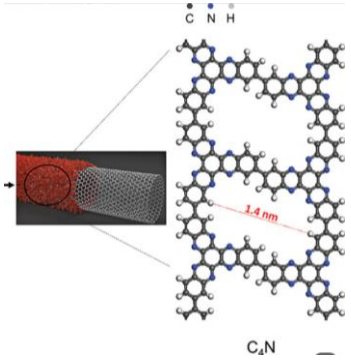	**C_4N-50% MWCNT**: conductive additive: PVDF (7:2:1)	5 M H_2SO_4 (0.9 mg cm^{-2})	422 mAh g^{-1} (6 e^-)	−0.1–0.8 V vs. Ag/AgCl	214.5 mAh g^{-1} at 1 A g^{-1}	191.6 mAh g^{-1} at 60 A g^{-1}	94.8% after 2000 cycles at 5 A g^{-1}	39

Structure	Composition of Electrode (active material: conductive carbon: binder)	Electrolyte (Mass Loading)	Theoretical Capacity (Electron Transfer)	Voltage Window (V)	Initial Capacity at Lowest Rate Reported	Reversible Capacity at Highest Rate Reported	Capacity Retention at Highest Rate	Ref.
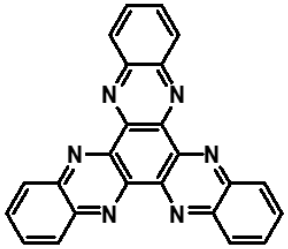	**HATN**: KB: PTFE (6:3:1)	9.5 M H_3PO_4 (2 mg cm^{-2})	418 mAh g^{-1} (6 e^-)	0–0.2 V vs. Ag/AgCl	255 mAh g^{-1} at 0.5 A g^{-1}	202 mAh g^{-1} at 20 A g^{-1}	90% after 5000 cycles at 10 A g^{-1}	40
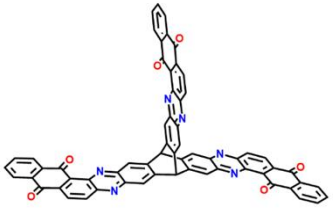	**DBH**: acetylene black: PVDF (7:2:1)	1 M H_2SO_4 (2 mg cm^{-2})	338 mAh g^{-1} (12 e^-)	0.2–0.5 V vs. Ag/AgCl	277.9 mAh g^{-1} at 1 A g^{-1}	207.8 mAh g^{-1} At 100 A g^{-1}	90% after 8000 cycles at 4 A g^{-1}	41
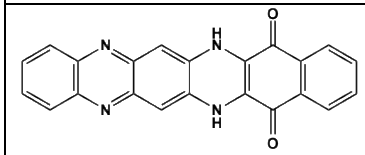	**DHQPD**: conductive additive: PTFE (7:2:1)	5 M H_2SO_4 (2 mg cm^{-2})	294.2 mAh g^{-1} (4 e^-)	0.2–0.35 V vs. Ag/AgCl	182.6 mAh g^{-1} at 0.5 A g^{-1}	132 mAh g^{-1} at 5 A g^{-1}	88.7% after 5000 cycles at 5 A g^{-1}	42

Structure	Composition of Electrode (active material: conductive carbon: binder)	Electrolyte (Mass Loading)	Theoretical Capacity (Electron Transfer)	Voltage Window (V)	Initial Capacity at Lowest Rate Reported	Reversible Capacity at Highest Rate Reported	Capacity Retention at Highest Rate	Ref.
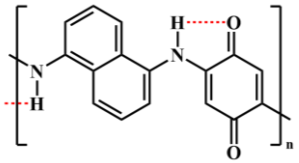 HMND	**HMND**: KB: PTFE (6:3:1)	2 M H_2SO_4 + 2 M $MnSO_4$ (2 mg cm^{-2})	206.2 mAh g^{-1} (2 e^-)	0.1–0.5 V vs. Ag/AgCl	176.4 mAh g^{-1} at 0.2 A g^{-1}	100.9 mAh g^{-1} at 80 A g^{-1}	76% after 7500 cycles at 4 A g^{-1}	43
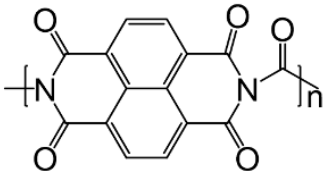 PNTCDA	**PNTCDA**: KB: PTFE (6:3:1)	2 M H_2SO_4 + 2 M $MnSO_4$ (3 mg cm^{-2})	183 mAh g^{-1} (2 e^-)	–0.2–0.6 V vs. Ag/AgCl	101 mAh g^{-1} at 1 A g^{-1}	26 mAh g^{-1} at 100 A g^{-1}	66% after 3500 cycles at 1 A g^{-1}	44
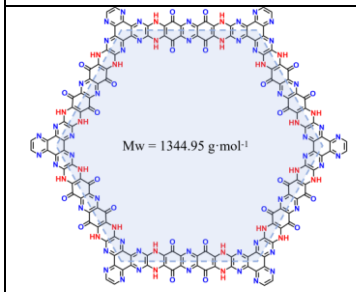	**TAPT-HAT-CO**: Super-P: PVDF (7:2:1)	0.5 M H_2SO_4 2.5 ± 0.05 mg/cm^2	239.1 mAh g^{-1} (12 e^-)	–0.6–0.1 V vs. Ag/AgCl	201 mAh g^{-1} at 2 A g^{-1}	~180 mAh g^{-1} at 5 A g^{-1}	91.3% after 2000 cycles at 2 A g^{-1}	45

Structure	Composition of Electrode (active material: conductive carbon: binder)	Electrolyte (Mass Loading)	Theoretical Capacity (Electron Transfer)	Voltage Window (V)	Initial Capacity at Lowest Rate Reported	Reversible Capacity at Highest Rate Reported	Capacity Retention at Highest Rate	Ref.
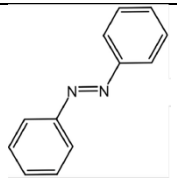 AB	**AB**: Super-P: PTFE (5:4:1)	2 M KOH 4–5 mg/cm^2	290 mAh g^{-1} (2 e$^-$)	–1.0– (–0.1) V vs. Hg/HgO [–1.1– (–0.2) V vs. Ag/AgCl]	234 mAh g^{-1} at 0.5 A g^{-1}	151 mAh g^{-1} at 10 A g^{-1}	~65% after 12500 cycles at 5 A g^{-1}	46
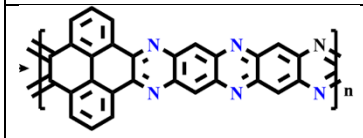 PPHZ	**PPHZ**: acetylene black: PVDF (7:2:1)	1 M H_2SO_4 1.5 mg/cm^2	354 mAh g^{-1} (4 e$^-$)	–0.2–0.6 V vs. Ag/AgCl*	273 mAh g^{-1} at 0.5 A g^{-1}	91.2 mAh g^{-1} at 100 A g^{-1}	93.6% after 6000 cycles at 8 A g^{-1}	47

Note: The asterisk (*) indicates that the reported value was obtained from the rate capability curve, cyclic voltammogram, or galvanostatic charge/discharge profile presented in the corresponding literature.

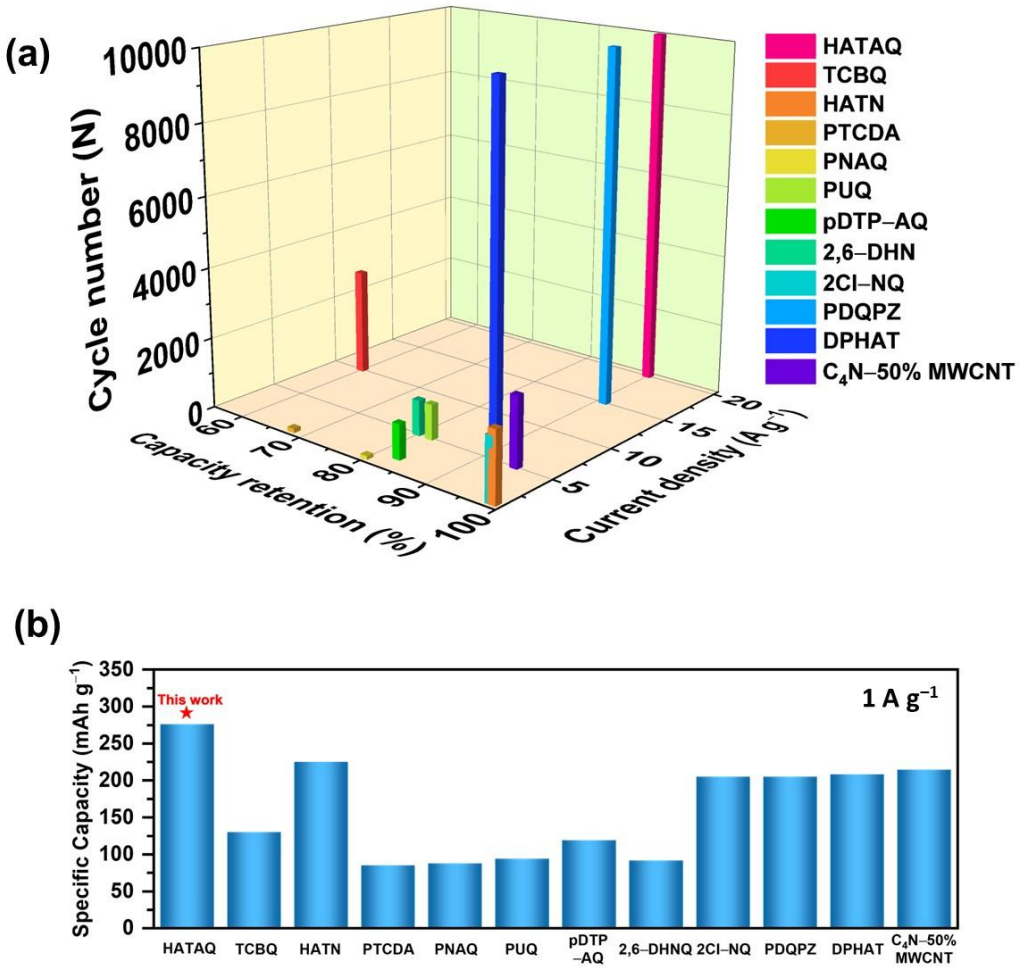

Fig. S29 Performance comparison of aqueous proton-based half cells reported in the literature. (a) Performance in terms of % capacity retention with cycle number at the highest current density reported. (b) Capacity values at 1 A g^{-1} (TCBQ,[19] HATN,[24] PTCDA,[25] PNAQ,[26] PUQ,[27] pDTP-AQ,[28] 2,6-DHNQ,[29] 2Cl-NQ,[30] PDQPZ,[31] DPHAT,[32] and C_4N-50% MWCNT)[39].

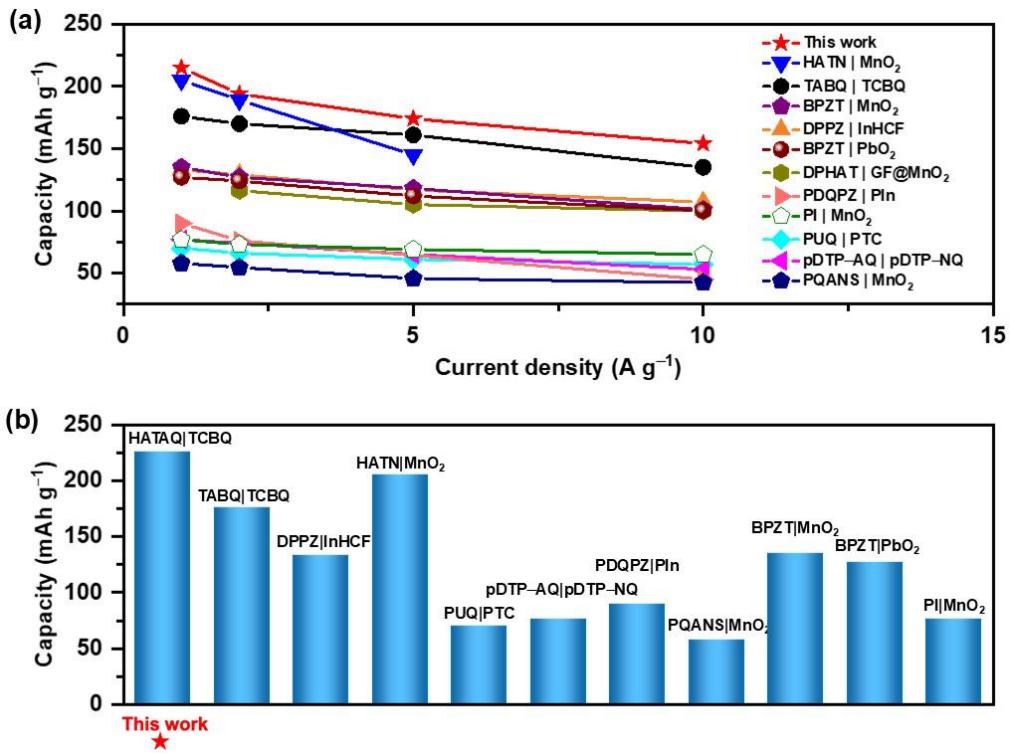

Fig. S30 Performance comparison for aqueous proton-based full cells. (a) capacity as a function of current density (1–10 A g^{-1}). (b) Comparison of full cells at 1 A g^{-1} (HATN/MnO_2,[24] TABQ/TCBQ,[18] BPZT/MnO_2,[37] DPPZ/InHCF,[21] BPZT/PbO_2,[37] DPHAT/GF@MnO_2,[32] PDQPZ/PIn,[31] PI/MnO_2,[44] PUQ/PTC,[27] pDTP-AQ/pDTP-NQ,[28] PQANS/MnO_2)[34].

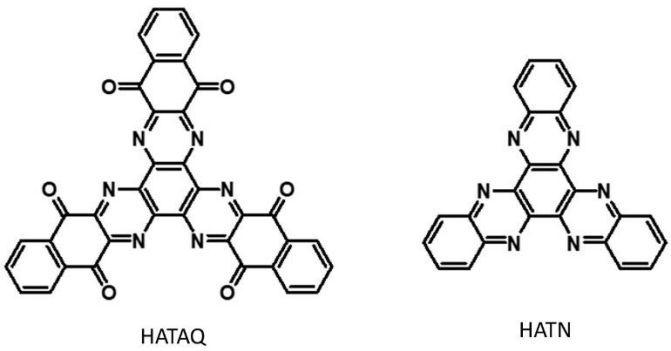

Fig. S31 Chemical structures of HATAQ and HATN.

References

(1) Wu, M.-S.; Luu, N. T. H.; Chen, T.-H.; Lyu, H.; Huang, T.-W.; Dai, S.; Sun, X.-G.; Ivanov, A. S.; Lee, J.-C.; Popovs, I.; Kaveevivitchai, W. Supramolecular Self-Assembled Multi-Electron-Acceptor Organic Molecule as High-Performance Cathode Material for Li-ion Batteries, *Adv. Energy Mater.* **2021***, 11,* 2100330.

(2) Shaoa, H.; Lina, Z.; Xua, K.; Tabernaa, P.-L.; Simon, P. Electrochemical Study of Pseudocapacitive Behavior of $Ti_3C_2T_x$ MXene material in aqueous electrolytes, *Energy Storage Mater.* **2019**, *18*, 456–461.

(3) Fleischmann, S.; Mitchell, J. B.; Wang, R.; Zhan, C.; Jiang, D.-E.; Presser, V.; Augustyn, V. Pseudocapacitance: From Fundamental Understanding to High Power Energy Storage Materials, *Chem. Rev*. **2020**, *120*, 6738–6782.

(4) Ren, W.; Qin, M.; Zhu, Z.; Yan, M.; Li, Q.; Zhang, L.; Liu D.; Mai, L. Activation of Sodium Storage Sites in Prussian Blue Analogues via Surface Etching, *Nano Lett.* **2017**, *17*, 4713–4718.

(5) Lee, Y.-S.; Ryu, K.-S. Study of the Lithium Diffusion Properties and High Rate Performance of $TiNb_6O_{17}$ as an Anode in Lithium Secondary Battery, *Sci. Rep.* **2017**, *7*, 16617.

(6) Luu, N. T. H.; Ivanov, A. S.; Chen, T.-H.; Popovs, I.; Lee, J.-C.; Kaveevivitchai, W. Proton-Enabled Biomimetic Stabilization of Small-Molecule Organic Cathode in Aqueous Zinc-Ion Batteries, *J. Mater. Chem. A* **2022***, 10,* 12371–12377.

(7) Russell, J. C.; Posey, V. A.; Gray, J.; May, R.; Reed, D. A.; Zhang, H.; Marbella, L. E.; Steigerwald, M. L.; Yang, Y.; Roy, X.; Nuckolls, C.; Peurifoy, S. R. High-performance Organic Pseudocapacitors via Molecular Contortion, *Nat. Mater*. 2021, **20**, 1136–1141.

(8) Wang, J.; Polleux, J.; Lim, J.; Dunn, B. Pseudocapacitive Contributions to Electrochemical Energy Storage in TiO_2 (Anatase) Nanoparticles, *J. Phys. Chem. C* **2007**, *111*, 14925–14931.

(9) Liu, T.-C.; Pell, W. G.; Conway, B. E.; Roberson, S. L. Behavior of Molybdenum Nitrides as Materials for Electrochemical Capacitors: Comparison with Ruthenium Oxide, *J. Electrochem. Soc*. **1998**, *145*, 1882.

(10) Ko, J. S.; Sassin, M. B.; Rolison, D. R.; Long, J. W. Deconvolving Double-layer, Pseudocapacitance, and Battery-like Charge-storage Mechanisms in Nanoscale $LiMn_2O_4$ at 3D Carbon Architectures, *Electrochim. Acta* **2018**, *275*, 225.

(11) Brezesinski, T.; Wang, J.; Polleux, J.; Dunn, B.; Tolbert, S. H. Templated Nanocrystal-Based Porous TiO_2 Films for Next-Generation Electrochemical Capacitors, *J. Am. Chem. Soc*. **2009**, *131*, 1802–1809.

(12) Brezesinski, T.; Wang, J.; Senter, R.; Brezesinski, K.; Dunn, B.; Tolbert, S. H. On the Correlation between Mechanical Flexibility, Nanoscale Structure, and Charge

Storage in Periodic Mesoporous CeO_2 Thin Films, *ACS Nano* **2010**, *4*, 967–977.
(13) Brezesinski, K.; Wang, J.; Haetge, J.; Reitz, C.; Steinmueller, S. O.; Tolbert, S. H.; Smarsly, B. M.; Dunn, B.; Brezesinski, T. Pseudocapacitive Contributions to Charge Storage in Highly Ordered Mesoporous Group V Transition Metal Oxides with Iso-Oriented Layered Nanocrystalline Domains, *J. Am. Chem. Soc*. **2010**, *132*, 6982–6990.
(14) Augustyn, V.; Come, J.; Lowe, M. A., Kim, J. W.; Taberna, P.-L.; Tolbert, S. H.; Abruña, H. D.; Simon, P.; Dunn, B. High-rate Electrochemical Energy Storage Through Li^+ Intercalation Pseudocapacitance, *Nat. Mater*. **2013**, *12*, 518–522.
(15) Ardizzone, S.; Fregonara, G.; Trasatti, S. "Inner" and "Outer" Active Surface of RuO_2 Electrodes, *Electrochim. Acta* **1990**, *35*, 263–267.
(16) Baronetto, D.; Krstajić, N.; Trasatti S. Reply to "Note on a Method to Interrelate Inner and Outer Electrode Areas" by H. Vogt, *Electrochim. Acta* **1994**, *39*, 2359–2362.
(17) Jing, R.; He, J.; Hu, L.; Yang, J.; Yan, C.; Shi, M. A Holomolecule Conjugated and Electron Delocalized Organic Compound for Superior Proton-Storage Redox Capability, *Chem. Eng. J.* **2023**, *477*, 147169.
(18) Wu, S.; Taylor, M.; Guo, H.; Wang, S.; Han, C.; Vongsvivut, J.; Meyer, Q.; Sun, Q.; Ho, J.; Zhao, C. A High-Capacity Benzoquinone Derivative Anode for All-Organic Long-Cycle Aqueous Proton Batteries, *Angew. Chem. Int. Ed.* **2024**, *63*, e202412455.
(19) Yue, F.; Tie, Z.; Deng, S.; Wang, S.; Yang, M.; Niu, Z. An Ultralow Temperature Aqueous Battery with Proton Chemistry, *Angew. Chem. Int. Ed.* **2021**, *60*, 13882–13886.
(20) Yu, J.; Li, J.; Leong, Z. Y.; Li, D.-s.; Lu, J.; Wang, Q.; Yang, H. Y. A Crystalline Dihydroxyanthraquinone Anodic Material for Proton Batteries, *Mater. Today Energy* **2021**, *22*, 100872.
(21) Qiao, J.; Qin, M.; Shen, Y. M.; Cao, J.; Chen, Z.; Xu, J. A Rechargeable Aqueous Proton Battery Based on a Dipyridophenazine Anode and an Indium Hexacyanoferrate Cathode, *Chem. Commun.* **2021**, *57*, 4307–4310.
(22) Yang, X.; Ni, Y.; Lu, Y.; Zhang, Q.; Hou, J.; Yang, G.; Liu, X.; Xie, W.; Yan, Z.; Zhao, Q.; Chen, J. Designing Quinone-Based Anodes with Rapid Kinetics for Rechargeable Proton Batteries, *Angew. Chem. Int. Ed.* **2022**, *61*, e202209642.
(23) Su, Z.; Tang, J.; Chen, J.; Guo, H.; Wu, S.; Yin, S.; Zhao, T.; Jia, C.; Meyer, Q.; Rawal, A.; Ho, J.; Fang, Y.; Zhao, C. Co-Insertion of Water with Protons into Organic Electrodes Enables High-Rate and High-Capacity Proton Batteries, *Small Struct.* **2023**, *4*, 2200257.
(24) Dai, Y.; Yan, X.; Zhang, J.; Wu, C.; Guo, Q.; Luo, J.; Hu, M.; Yang, J. High-Capacity Proton Battery Based on π-Conjugated N-Containing Organic Compound, *Electrochim. Acta* **2023**, *442*, 141870.
(25) Wang, X.; Bommier, C.; Jian, Z.; Li, Z.; Chandrabose, R. S.; Rodriguez-Perez, I. A.; Greaney, P. A.; Ji, X. Hydronium-Ion Batteries with Perylenetetracarboxylic

Dianhydride Crystals as an Electrode, *Angew. Chem. Int. Ed.* **2017**, *56*, 2909–2913.
(26) Sun, T.; Du, H.; Zheng, S.; Shi, J.; Yuan, X.; Li, L.; Tao, Z. Bipolar Organic Polymer for High Performance Symmetric Aqueous Proton Battery, *Small Methods* **2021**, *5*, e2100367.
(27) Zhu, M.; Zhao, L.; Ran, Q.; Zhang, Y.; Peng, R.; Lu, G.; Jia, X.; Chao, D.; Wang, C. Bioinspired Catechol-Grafting PEDOT Cathode for an All-Polymer Aqueous Proton Battery with High Voltage and Outstanding Rate Capacity, *Adv. Sci.* **2022**, *9*, e2103896.
(28) Wang, X.; Zhou, J.; Tang, W. Poly(dithieno[3,2-b:2',3'-d]pyrrole) Twisting Redox Pendants Enabling High Current Durability in All-Organic Proton Battery, *Energy Storage Mater.* **2021**, *36*, 1–9.
(29) Zhao, G.; Yan, X.; Dai, Y.; Xiong, J.; Zhao, Q.; Wang, X.; Yu, H.; Gao, J.; Zhang, N.; Hu, M.; Yang, J. Searching High-Potential Dihydroxynaphthalene Cathode for Rocking-Chair All-Organic Aqueous Proton Batteries, *Small* **2024**, *20*, e2306071.
(30) Lu, H.; Yu, J.; Zhang, J.; Dong, C.; Song, W.; Ye, F.; Zhang, W.; Li, Y.; Yang, L.; Li, M.; Xu, L. Designing p-π Conjugated Naphthoquinone-Derivatives as High-Performance Cathodes for Aqueous Proton Batteries, *Adv. Funct. Mater.* **2025**, 2421858.
(31) He, J.; Zhao, Y.; Yan, C.; Jing, R.; Wang, R.; Shi, M. Highly Redox-Active Polymer with Extensive Electron Delocalization and Optimized Molecular Orbitals for Extraordinary Proton Storage, *Chem. Eng. J.* **2023**, *470*, 144204.
(32) Yang, J.; Wang, H.; Cui, Y.; Shi, M.; Yan, C. Engineered N-Heterocyclic Molecule with Abundant Imine Sites Induced Hydrogen Bonding for High-Rate Aqueous Proton Batteries, *Chem. Eng. J.* **2025**, *514*, 163396.
(33) Jiang, H.; Shin, W.; Ma, L.; Hong, J. J.; Wei, Z.; Liu, Y.; Zhang, S.; Wu, X.; Xu, Y.; Guo, Q.; Subramanian, M. A.; Stickle, W. F.; Wu, T.; Lu, J.; Ji, X. A High-Rate Aqueous Proton Battery Delivering Power Below −78 °C Via an Unfrozen Phosphoric Acid, *Adv. Energy Mater.* **2020**, *10*, 2000968.
(34) Yang, J.; Shao, P.; Zhao, X.; Liao, Y.; Yan, C. Quinone-Amine Polymer Nanospheres with Enhanced Redox Activity for Aqueous Proton Storage, *J. Colloid Interface Sci.* **2023**, *650*, 1811–1820.
(35) Miao, Y.; Jin, W.; Qin, M.; Shen, Y.-M.; Chen, Y.; Wu, T.-R.; Wu, D.-Y.; Xu, J.; Cao, J. Redox-Active Poly(Imide-Quinone) Covalent Organic Framework Anodes for High-Efficient and Durable Aqueous Proton Batteries, *Chem. Eng. J.* **2024**, *485*, 149986.
(36) Wang, Y.; Wang, C.; Wang, W.; Zhang, Y.; Guo, Z.; Huang, J.; Yan, L.; Ma, J.; Wang, Y. Organic Hydronium-Ion Battery with Ultralong Life, *ACS Energy Lett.* **2023**, *8*, 1390–1396.
(37) Wang, C.; He, D.; Wang, H.; Guo, J.; Bao, Z.; Feng, Y.; Hu, L.; Zheng, C.; Zhao, M.; Wang, X.; Wang, Y. Symmetrical Design of Biphenazine Derivative Anode for

Proton Ion Batteries with High Voltage and Long-Term Cycle Stability, *Adv. Sci.* **2024**, *11*, e2401314.
(38) Shen, D.; Rao, A. M.; Zhou, J.; Lu, B. High-Potential Cathodes with Nitrogen Active Centres for Quasi-Solid Proton-Ion Batteries, *Angew. Chem. Int. Ed.* **2022**, *61*, e202201972.
(39) Yang, M.; Zhao, Q.; Ma, H.; Li, R.; Wang, Y.; Zhou, R.; Liu, J.; Wang, X.; Hao, Y.; Ren, J.; Zheng, Z.; Zhang, N.; Hu, M.; Luo, J.; Yang, J. Integrated Uniformly Microporous C(4) N/Multi-Walled Carbon Nanotubes Composite toward Ultra-Stable and Ultralow-Temperature Proton Batteries, *Small* **2023**, *19*, e2207487.
(40) Xu, Q.; Liu, L.; Chen, K.; Xiang, Y.; Liu, X.; Yu, H.; Zhang, L.; Yan, L.; Shu, J. A Rocking-Chair Type All-Organic Proton Battery Operated at Ultralow Temperature. *Mat. Chem. Front.* **2025**, *9*, 3264–3273.
(41) Liu, H.; Yang, J.; Yan, C.; Jing, R.; Yang, J.; Ni, C.; Shi, M.; Guo, J.; Zhao, J.; Wu, X. Geometric Preorganization Enables Entropy-Constrained Proton Migration for Ultrafast and Stable Aqueous Proton Batteries. *Angew. Chem. Int. Ed.* **2026**, *65*, 11.
(42) Ju, N.; Wang, P.; Liu, Z.; Wang, Y.; Liu, Z.; Wang, Y.; Hao, S.; Jia, M.; Luo, S.; Shao, D.; et al. Synthesizing Organic Electrode with Low-Cost Bulk Chemicals to Enable High-Efficiency and Durable Aqueous Proton Battery. *J. Energy Storage* **2026**, *152*, 9.
(43) Liu, X.; Tang, J.; Bin, D.; Li, C.; Su, L.; Qin, W.; Chen, X.; Ge, Y.; Ge, R.; Yang, B.; et al. Intramolecular Hydrogen Bonds Enhanced Quinone-Based Anode for High-Performance Aqueous Proton Batteries. *Adv. Mater.* **2026**, *38*, 11.
(44) Han, W.; Li, M.; Ma, Y.; Yang, J. Dianhydride-Based Polyimide as Organic Electrode Materials for Aqueous Hydronium-Ion Battery. *Electrochim. Acta* **2022**, *403*, 9.
(45) Xu, Y.; Wang, Z.; Feng, Y.; Wang, Y. Dual-Redox Conjugated Bipolar Covalent Organic Framework Enables High-Voltage Symmetric Proton Batteries. *Angew. Chem. Int. Ed.* **2026**, *65*, e9770638.
(46) Dong, S.; Ren, H.; Yang, J.; Zhang, J.; Cao, Z.; Long, L.; Xu, Z.; Shao, H.; Zhang, X. An Aqueous Proton Battery under Alkaline Electrolyte. *Energy Storage Mater.* **2025**, *74*, 8.
(47) Wang, R.; He, J.; Yan, C.; Jing, R.; Zhao, Y.; Yang, J.; Shi, M.; Yan, X. A Long-Range Planar Polymer with Efficient π-Electron Delocalization for Superior Proton Storage. *Adv. Mater.* **2024**, *36*, 12.